/IN-20
9926
84 P

Performance of a Quasi-Steady, Multi Megawatt, Coaxial Plasma Thruster

Jay T. Scheuer, Kurt F. Schoenberg, Ivars Henins, Richard A. Gerwin,
Ronald W. Moses, Jr., Jose A. Garcia, and Robert F. Gribble
Los Alamos National Laboratory
Los Alamos, New Mexico

Robert P. Hoyt
University of Washington
Seattle, Washington

and

Dorwin C. Black and Robert M. Mayo
North Carolina State University
Raleigh, North Carolina

April 1994

(NASA-CR-195311) PERFORMANCE OF A
QUASI-STEADY, MULTI MEGAWATT,
COAXIAL PLASMA THRUSTER Final
Report (LANL) 84 p

N94-32970

Unclas

G3/20 0009926

LA-UR- 93-4100

Title: Performance of a Quasi-Steady, Multi-Megawatt, Coaxial Plasma Thruster

Author(s): Jay T. Scheuer
Kurt F. Schoenberg
Ivars Henins
Richard A. Gerwin
Jose A. Garcia
Robert F. Gribble
Robert P. Hoyt
Dorwin C. Black
Robert M. Mayo
Ronald W. Moses, Jr.

Submitted to: NASA Contract Report

Los Alamos
NATIONAL LABORATORY

Submitted for NASA Contractor Report:

Performance of a Quasi-Steady, Multi-Megawatt, Coaxial Plasma Thruster

by

Jay T. Scheuer, Kurt F. Schoenberg, Ivars Henins, Richard A. Gerwin,
Ronald W. Moses Jr, Jose A. Garcia, and Robert F. Gribble
Los Alamos National Laboratory, Los Alamos, NM 87545

Robert P. Hoyt
*Aerospace and Energetics Research Program,
University of Washington, Seattle, WA 98195*

Dorwin C. Black, Robert M. Mayo
*Department of Nuclear Engineering,
North Carolina State University, Raleigh, NC 27695*

CONTENTS

Performance of a Quasi-Steady, Multimegawatt, Coaxial Plasma Thruster

by
Jay T. Scheuer, Kurt F. Schoenberg, Ivars Henins, Richard A. Gerwin,
Ronald W. Moses, Jr., Jose A. Garcia, and Robert F. Gribble
Los Alamos National Laboratory, Los Alamos, NM 87545
Robert P. Hoyt
Aerospace and Energetics Research Program
University of Washington, Seattle, WA 98195
Dorwin C. Black, Robert M. Mayo
Department of Nuclear Engineering,
North Carolina State University, Raleigh, NC 27695

Abstract

The Los Alamos National Laboratory Coaxial Thruster Experiment (CTX) has been upgraded to enable the quasi-steady operation of magnetoplasmadynamic (MPD) type thrusters at power levels from 2 to 40 MW for 10 ms. Diagnostics include an 8-position, 3-axis magnetic field probe to measure magnetic field fluctuations during the pulse, a triple Langmuir probe to measure ion density, electron temperature and plasma potential and a time-of-flight neutral particle spectrometer to measure specific impulse. Here we report on the experimental observations and associated analysis and interpretation of long-pulse, quasi-steady, coaxial thruster performance in the CTX device.

I. INTRODUCTION

Magnetoplasmadynamic (MPD) thrusters constitute potentially attractive, high-specific-impulse propulsion engines that are compact and mechanically robust. Recent analysis by Myers et. al., 1993 has shown that pulsed MPD thruster systems could have a dramatic near-term impact on orbit raising missions. For payloads of between 1000 and 2000 kg, Myers concluded that pulsed MPD thrusters, using present generation power conditioning components and envisaged solar electric space power systems, could substantially reduce launch vehicle mass and associated launch cost for LEO to GEO orbit transfers. Of course, central to this application is the development of an efficient, reliable, and long-lived magnetohydrodynamic (MHD) thruster.

In 1991, the NASA Lewis Research Center initiated a research program at the Los Alamos National Laboratory to investigate the power utilization in a large, high-power, coaxial plasma accelerator, CTX, with a view to enhancing MHD thruster performance. This work (Schoenberg et al., 1991, Schoenberg, et al., 1993) qualitatively showed the beneficial effects of an applied magnetic nozzle on coaxial plasma thruster performance. Here, an unconventional and unoptimized magnetic geometry was able to markedly effect control over the anode sheath potential drop. Moreover, this was accomplished without significantly modifying the annular magnetic nozzle, as inferred from the simultaneous observation that the plasma exhaust velocity was in excellent agreement with the predictions of MHD nozzle flow theory.

In this paper, we present further research on thruster performance optimization. This research utilized the upgraded Los Alamos CTX facility that is capable of sustaining 10-ms, 2- to 40-MW, quasi-steady-state discharges. This capability represents a substantial improvement over the previously reported results, in which the thruster discharges were not "flat-topped" and were only 1.0 ms in duration. The crux of this research is that it points to coaxial plasma thruster operational designs and regimes that support the efficacy of MPD thrusters for recently prescribed solar electric orbit transfer vehicle and planetary exploration missions.

The coaxial plasma thruster can be viewed as an evolutionary variation of the MPD thruster in which an annular magnetic nozzle is used to optimize thruster performance. The annular nozzle is unconventional with respect to canonical applied-field MPD thrusters, in that the nozzle shape is carefully controlled and the applied-field magnitude is of order the self field. A proper nozzle configuration can enhance thruster performance by controlling the "magnetic connection" across the electrode sheaths and concomitantly, minimizing anode fall and electrode arcing. Furthermore, the use of a proper nozzle-field shape can produce smooth, efficient acceleration and detachment of the plasma propellant.

The Myers 1993 study assumed a thruster efficiency of 50%, lifetimes between 2500 to 6000 hours, and specific impulses between 2000 and 5000 seconds in hydrogen or deuterium. Clearly, future research is necessary to quantitatively demonstrate this performance. However, the research reported herein supports the expectation that nozzle-based coaxial plasma thrusters can achieve these demanding performance requirements.

II. CTX FACILITY

A. Introduction

The CTX facility consists of a 1 m long, 0.56 m diameter coaxial plasma thruster, a 1.5 m diameter, 5 m long stainless steel vacuum tank with turbomolecular pumping,

2

a 2 MJ capacitor bank, and a PC/workstation based process control, data acquisition and data analysis system. In previous work, (Schoenberg 1993a, b) this facility was not optimized for long pulse thruster operation, which resulted in round top voltage and current waveforms with a 1 ms discharge. In order to verify the true quasi- steady state operation of the thruster, a number of steps have been taken to upgrade the experimental facility as described below. A schematic of the CTX coaxial plasma thruster is shown in Fig. 1. The thruster consists of two coaxial, stainless steel, tungsten-coated electrodes. The inner and outer electrodes are 1 m long and have diameters of 0.37 m and 0.56 m, respectively.

B. Facility Upgrade

1. Pulse Forming Network The 2 MJ capacitor bank has been reconfigured as a lumped-constant transmission line capable of providing a flat-top, 10 ms discharge delivering from 2 to 40 MW to the thruster. A schematic of the five stage, pulse forming network is shown in Fig. 2. The capacitors are charged to the desired level (up to 10 kV), and the gas inlet valve (described below) is fired. After a 10 ms delay to allow the gas to reach the thruster, the start ignitron switch (S1 in Fig. 2) is fired. After an additional 15 ms, the crowbar ignitron switch (S2) is fired, terminating the discharge.

2. Thruster Isolation

In previous work (Schoenberg, et al. 1993a, b), a large amount of the discharge current flowed from the center electrode (cathode) to the vacuum tank wall, since the outer electrode (anode) was electrically connected to the wall. This issue has been addressed by the addition of an insulating, glass flange that connects the thruster to the vacuum tank mechanically, but not electrically. This encourages the current to flow between the electrodes, rather than from the cathode to the vacuum tank wall.

3. Gas Inlet Valve

The working gas is supplied to the thruster throughout the discharge at a controlled rate. The maximum flow rates achievable are 40 g/s in argon and 7 g/s in helium and deuterium. The thruster has twelve gas inlet ports located approximately in the midplane of the barrel. As shown in Fig. 3, six of these are used to inject the working gas. A single, bellows-sealed, stainless steel, pneumatically opened valve (Nupro SS-4BK 91NC) admits the gas from the reservoir into the manifold. This pneumatic valve is opened with a helium gas pulse (at 125 psig) supplied by a capacitor-discharge-(6-uF at 300-V) driven, SCR-switched, electrically operated valve (Skinner A3LB2262-CA2; 115-VAC coil). Following the Nupro valve, the

gas flows through a manifold of six equal-length (80-cm) 4.6-mm I.D. stainless steel tubes and enters the thruster through the gas ports. These narrow tubes act as sonic orifices so that pressure build up in the thruster does not affect the instantaneous gas flow rate. At the end of a typical discharge the tank pressure rises to 100 mTorr. A fast (few microsecond response time) piezoelectric pressure gauge is used to measure the duration of the working-gas pulse at the outlet of the valve and the inlet to the manifold. A typical helium pressure pulse signal is shown in Fig. 4. The duration (as measured at FWHM) of the gas pulse varied from 12.0 ms at 1,564 Torr reservoir pressure to 18.1 ms at 7,500 Torr. Above that pressure the valve does not seal. The pressure drop in the reservoir was typically about 2.5% during a discharge.

The total gas quantity is calculated from the pressure rise, as measured with a capacitance manometer, in the 8,141-l volume CTX vacuum tank. When the mass increase of gas in the tank is divided by the pulse width for the respective reservoir pressures, the result is linear with pressure (with a slope of 8.9×10^{-4} g/(sec Torr) for helium), indicating constant flow over the gas pulse duration (Fig. 5). This calibration process was repeated for the other gases used in these experiments.

4. Applied Magnetic Field The center electrode (cathode) contains a solenoidal coil that produces an applied $B_{r,z}$ field (the nozzle field). The coil is driven by a 50 volt, 300 amp DC power supply. The supply is energized 3 seconds before the discharge which allows the nozzle field to fully achieve its vacuum configuration. However, the interaction of the flowing plasma with the applied field distorts the vacuum field shape and is believed to form a rudimentary magnetic nozzle (Schoenberg, et al. 1991, Schoenberg, et al. 1992) (see discussion of magnetic fluctuation measurements below). This unoptimized $B_{r,z}$ field configuration is unconventional within MPD thruster research in that some of the applied magnetic field lines are intercepted by both electrodes, with a connection length estimated to be on the order of several times the electrode spacing $\Delta \sim 0.1$ m. Thus, from the MPD standpoint, the CTX plasma thruster is unusual with regard not only to size and power level, but also with regard to the applied magnetic configuration. Future research will focus on optimizing the $B_{r,z}$ field configuration with respect to optimizing thruster performance.

C. Diagnostics

1. Current and Voltage The potential of the thruster electrodes with respect to the grounded vacuum tank was measured using two 1:1000 voltage dividers and the result was subtracted to yield the thruster voltage drop. The thruster current was measured using a Rogowski loop connected to a passive, 500 μs integrator. The "droop" in this signal was corrected by the data acquisition computer. These signals were digitized at the rate of 200 kHz using a LeCroy 6810 waveform recorder.

2. Magnetic Fluctuation Probe An array of three-axis magnetic probes to measure magnetic field fluctuations in the exhaust plume consists of 24 coils wrapped on a 38 cm long, 0.64 cm diameter Acetal form. At 8 positions, each 2.54 cm apart, three mutually perpendicular coils were wound to measure magnetic field in the $\hat{r}$, $\hat{\theta}$, and $\hat{z}$ directions. The turn area of each of the coils is roughly 5 cm^2. The probe was calibrated using a Helmholtz coil. The ends of all the coils are brought out as twisted pairs to prevent unwanted magnetic pickup. A 0.025-cm-thick stainless steel jacket acts both to protect the probe from the plasma and to provide a vacuum boundary. The thickness of the jacket is sufficiently small to allow the probe to respond to magnetic oscillations at frequencies exceeding 100 kHz. The signals are digitized at the rate of 250 kHz using a LeCroy 8210 waveform recorder. Both the acetal form and the coils are wrapped with high voltage tape to provide electrical insulation between the coils and the stainless steel jacket.

The jacket containing the probe is connected, via a 90 degree elbow, to a sliding extension and vacuum feed through which allows 1.2 m of probe travel (see Fig. 1). This allows the probe, when inserted through one of the side ports of the CTX vacuum chamber, to map the magnetic field in a 1.2 meter (radial) by 0.76 m (axial) area on the center plane of the vacuum chamber.

During thruster operation, a dc current is applied to the solenoid contained within the inner electrode. This current produces a steady state $B_{r,z}$ field which can not be detected by the B-dot probe. Therefore, in order to make an accurate determination of the total magnetic field profile during a discharge, the steady state component produced by the coil was mapped out beforehand using a Hall effect probe. This steady state field was then added to the time varying field measurement of the B-dot probe to obtain the total magnetic field at each spatial location.

Raw data obtained from the magnetic pickup probes was processed using an IDL data analysis program on the Sun workstation. Data for each position was first droop corrected using the expression

$$B(t) = -\left(\frac{RC}{A}\right)\left[V_c + \left(\frac{1}{RC}\right)\int_{t_0}^{t} V_c(\tau)d\tau\right] \quad .$$

This result, when added to the initial vacuum field, yields the total $\hat{r}$, $\hat{\theta}$, and $\hat{z}$ magnetic field strengths versus time for an array of points in the thruster exit plume. The primary simplifying assumption for all further data analysis was that of discharge axisymmetry. This assumption appears reasonable for positions close to the exit plane (<40 cm) and at times early in the discharge (a few milliseconds). At later times and positions far from the exit plane, this assumption appears to be less valid. This is evidenced by the fact that nonzero values of B_r and B_θ were observed on the axis of the tank late in the discharge. Using the axisymmetry assumption, magnetic flux surfaces were calculated by integrating the product of

5

B_z and dA radially

$$\Psi = \sum_{i=0}^{n} B_{z_i} \pi (r_{i+1/2}^2 - r_{i-1/2}^2) \ .$$

J_r and J_z were calculated from the curl of B. Because of the assumption of axisymmetry the equations for J_r and J_z simplify to:

$$J_r = -\frac{1}{\mu_0} \frac{\partial B_\phi}{\partial z} \quad \left[\frac{\partial B_z}{\partial \phi} = 0\right]$$

$$J_z = \frac{1}{\mu_0 r} \frac{\partial r B_\phi}{\partial r} \quad \left[\frac{\partial B_r}{\partial \phi} = 0\right]$$

3. Triple Langmuir Probe A moveable, triple Langmuir probe was used to measure electron temperature, ion density, and floating potential. The probe consisted of three tungsten wire electrodes (0.02 cm diam, 0.2 cm exposed length, 0.1 cm apart), fed through alternating holes in a six-bore alumina tube. A constant bias voltage was applied between two of the electrodes using a Kepco BOP 100-4M power supply, and the third electrode was allowed to float in the plasma. Typical bias voltages used were in the range of 45–75 V. The voltage between the floating probe and one of the biased probes provided a measurement of the electron temperature, and the current flowing through the biased probes, determined using a 50 Ω shunt resistor, provided a measurement of the ion density (Tilley, et al. 1990). All voltages were measured using Tektronix AM 501 operational amplifiers and digitized at the rate of 250 kHz using a LeCroy 8210 waveform recorder. The triple probe and the triple probe electronics were allowed to float relative to system ground by using an air-core isolation transformer to provide power to the electronics and by using fiber optic cable to transmit the measured voltages to the data acquisition equipment. Concurrently, the potential of the floating probe relative to the tank wall was measured to provide an estimation of the floating potential.

4. Time of Flight Neutral Particle Spectrometer The time of flight neutral particle analyzer (TOF/NPA) (Voss 1982, Mayo 1991) consists of a) a chopper wheel and stator assembly, b) a drift tube, and c) a detector and high-voltage gating system. High-energy neutrals are created via charge exchange reactions of accelerated ions with the background gas. These neutrals travel to a single-slit stator (2 cm × 0.025 cm), which acts as a collimator and vacuum break between the plasma discharge vessel and the TOF/NPA which must remain at high vacuum ($< 10^{-6}$ Torr). Immediately behind the stator is a titanium alloy (Ti-6Al-4V) chopper wheel (26.67 cm diam, 0.025 cm thick) which is rotated at ≈ 360 rps by a Leybold NT150 turbo pump. The chopper wheel has 16 radial slits (2 cm × 0.025 cm) that are laser-cut, circularly symmetric, and situated 8.5 mm from the wheel edge. Since the chopper and stator slits are the same width, the acceptance

6

function is triangular in time with a half opening time of 0.85 μs. After being chopped, neutrals then drift down a 197.5 cm evacuated drift tube where they are time/energy discriminated before striking the detector (Cu-Be plate and 20 stage electron multiplier). The TOF/NPA was positioned at the far end of the 5-m CTX vacuum tank (opposite the plasma thruster) to view into the barrel of the thruster. While this is the appropriate position for measuring the axial velocity, the detected neutral particle flux is required to drift the entire length of the CTX tank before entering the NPA drift tube. Because of this, spatial information is lost and timing information is slightly smeared ($\ell/v_z \simeq 20\mu$ s).

III. RESULTS AND DISCUSSION

A. Operating Regime

The operating regime was found for each gas by varying the propellant mass flow rate, bank charge voltage, and the current flowing through the applied field coil and observing thruster operation. The operating regime for helium is shown in Fig. 6. It was found that increasing the applied field increases the likelyhood that breakdown will occur at a given bank charge voltage and mass flow rate. Increasing the applied field also decreased the amount of time from the application of voltage to breakdown. The thruster was operational with no applied field at certain bank charge voltages and mass flow rates in argon. Previous short pulse operation did not require a minimum applied field to achieve breakdown since the capacitor bank was directly coupled to the thruster which produced a higher potential difference between the electrodes and aided breakdown. The discharge impedance, and fluctuation level varied with working gas as shown in Table I. The thruster impedance was observed to decrease with increasing applied field for all gases. (This effect is discussed below).

Table I. Thruster, Current, Voltage, Impedance, and Fluctuation Level for Various Gases: (argon #487; helium #274; deuterium #584)

Gas	Bank Charge Voltage (kV)	Mass Flow Rate (g/s)	Applied Field Current (A)	I (kA)	ΔI (A)	V (Volts)	ΔV (Volts)	Impedance (mΩ)
Ar	5.0	10	140	62	700	110	3	1.7 ± 0.05
He	5.0	1.25	140	59	400	202	20	3.4 ± 0.3
D2	5.0	1.25	177	51	90	273	38	5.3 ± 0.7

B. Steady State Operation

The time resolved thruster current and voltage are shown along with plasma density, electron temperature, plasma potential, and the three components of the magnetic field fluctuations from the upgraded CTX facility for a 6 MW helium discharge in Fig. 7. The density, temperature, and plasma potential were obtained using the triple Langmuir probe at a position 5.4 cm inside the thruster exit plane at a radial position equidistant from the anode and cathode. The plasma potential was obtained from the floating potential assuming a Maxwellian distribution of electrons. The magnetic field fluctuation measurements were obtained by the magnetic probe 1 cm outside the thruster exit at a radial location equidistant from the anode and cathode. The data indicate that the thruster reaches a time-average quasi-steady-state (flat-topped) operation roughly 3 ms into the discharge and remains in time-average steady state operation for approximately 10 ms.

C. Control of Anode Fall Potential

Fig. 8 shows the total thruster voltage (cathode voltage minus anode voltage) and anode fall voltage as a function of applied magnetic field. The anode fall voltage was inferred from the triple probe floating potential measured approximately 5 mm from the anode averaged over the current and voltage flat top and converted to plasma potential using the standard relation (F. F. Chen, 1965)

$$V_{\text{plasma}} = V_{\text{probe}} + \frac{kT_e}{2e} \ln \frac{2m_i}{\pi m_e} \quad ,$$

where T_e is the measured electron temperature, m_e is the electron mass and m_i is the ion mass. As the applied magnetic field is increased, the anode fall voltage decreases. Since some applied magnetic field lines intersect both electrodes, electrons can cross from cathode to anode at least partially along field lines. As the magnetic field is increased, the coupling of electrons to the anode also is increased, causing a decrease in the anode fall potential. This decrease in the anode fall potential is desirable from an efficiency standpoint since electrons incident on the anode then will carry with them less kinetic energy resulting in less anode heating and higher thruster efficiency.

As shown in Fig. 8, in the unoptimized applied magnetic field used for this work the total thruster voltage also decreases with increasing field. This "shorting out" of the thruster voltage is undesirable since it reduces the amount of E_r-field which is available for providing the $J_r B_\theta$ force driving the axial plasma acceleration. An optimized applied field would be one in which magnetic field lines connect the bulk of the plasma to the electrodes (thus reducing the fall potentials) without directly connecting the electrodes (thus reducing the "shorting out" effect). A schematic of such a field is shown in Fig. 9. Prototype field coils capable of producing such an applied field have been fabricated and are being used in ongoing research.

D. Magnetic Field Evolution

After determining the breakdown characteristics of helium in terms of reservoir gas fill pressure, bank voltage, and $B_{r,z}$ field strength, a series of discharges (#279–297) was performed under constant conditions to obtain magnetic field data. The main bank voltage for this first scan was set to 5 kV. Current through the $B_{r,z}$ coil was set to 140 amps. Reservoir pressure was maintained at 2500 torr. In order to obtain sufficient data to determine magnetic flux profiles, probe data from a series of discharges had to be recorded. The magnetic probe was repositioned before each discharge in order to record time-dependent magnetic field data at a different location. Because the axial spacing between coils on the probe was 5 cm, the probe was moved radially in steps of 5 cm between discharges. Bank charging voltage, initial steady state $B_{r,z}$ field strength, and initial gas reservoir pressure were each set to the same values before each shot in a series. Once time dependent field data was obtained for a grid of points all lying on a single plane in front of the thruster, the magnetic flux profiles could be determined as follows. Using the assumption of axisymmetry, the magnetic flux contained within a circle of radius r, centered on the axis of the CTX thruster is given by

$$\Psi(r,z) = \int_0^r B_z(r,z) 2\pi r dr.$$

However, because we only have field data for certain values of r, the integral given above must be approximated by a sum over the known values of B as

$$\Psi(r_i, z_j) = \sum_{k=1}^{i} B_z(r_k, z_j) \pi (r_{k+1/2}^2 - r_{k-1/2}^2).$$

Using this equation, $\Psi(r,z)$ for each point at which a magnetic field measurement was available could be calculated. A computer program was written to interpolate between the flux data to determine lines of constant magnetic flux. Flux plots were then produced to show how the shape of the magnetic flux profile evolved in time.

Figs. 10a-d show flux profiles at different time steps during a helium discharge. We see from 10a that before the discharge, between 2 and 3 mWb of flux cross the exit plane of the thruster. By 4 ms into the shot (see Fig. 10b), a quasi-steady state condition has been reached. There are only minor changes in the shape of the field lines over the next several milliseconds, as can be seen in Fig. 10c. Later in the discharge, Figs. 10c and 10d, we see that the flux begins to relax back towards the vacuum field configuration, as would be expected.

We can compare the time to reach a quasi-steady state (2 to 4 milliseconds) to the equilibration time of magnetic flux dragged downstream through the stainless steel anode. This equilibration results as a balance between the drag on the applied field by the moving plasma and the circumstance that the applied field is ultimately

anchored in its coil (assuming constant coil current). An approximate expression for the equilibration time of magnetic flux dragged downstream across the stainless steel anode of thickness δ has been derived and is given by

$$\tau_{\text{equil.}} = \mu_o L \delta / \eta_{\text{el.}},$$

where $\mu_o = 4\pi \cdot 10^{-7} \frac{\text{H}}{\text{m}}$ is the permeability of free space, $L \approx 10$ cm is a representative length along a field line to where it is anchored in the coil, δ is the thickness of the stainless steel anode (1/4 in.), and $\eta_{\text{el.}}^{-1}$ is the conductivity of stainless steel $(14 \cdot 10^5 \Omega^{-1} \text{m}^{-1})$. This $\tau_{\text{equil.}}$ may be identified as the (L/R) "settling time" of the transient azimuthal current fluctuations in the resistive electrodes, in which L constitutes the inductance of the large overall volume that encompasses the applied flux and its coil, and R represents the electrode resistance to azimuthal currents over the active length of the device.

Plugging in these numbers gives

$$\tau_{\text{equil.}} = (4\pi \cdot 10^{-7} \frac{\text{H}}{\text{m}})(10^{-1}\text{m})(6.35 \cdot 10^{-3}\text{m})(14 \cdot 10^5 \Omega^{-1}\text{m}^{-1}) = 1.12 \cdot 10^{-3}\text{s}.$$

Thus, this approximate magnetic-diffusion model yields a time on the order of 1 ms for the dragged magnetic flux to equilibrate through the stainless steel anode. (Taking into account the presence of a thin layer (~ 1 mm) of higher-conductivity tungsten on the electrode and a somewhat larger value for the length L moderately raises this time estimate.) Thus, this picture seems to coincide reasonably well with the observed times of 2 to 4 ms to reach quasi-steady state.

An important feature of the flux plots both before and during the quasi-steady state portion of these discharges is the diverging field line structure. As was shown in the work of Morozov and Solov'ev (1980), as well as Gerwin, et al., (1990), super-magnetosonic plasma flows are accelerated in annular diverging flow tube configurations. Therefore, if the plasma reaches the magnetosonic speed by the time it reaches the exit plane of the thruster, it will undergo further acceleration in the diverging nozzle configuration downstream of the thruster. However, in the CTX configuration being described here, the applied flux has not been optimized with respect to minimization of losses incurred in the plasma detachment process.

E. Plasma Density Evolution

As shown in Fig. 7, measurements made with the triple Langmuir probe indicate that the value of the electron density in the CTX thruster is lower during quasi-steady operation than during 1 ms pulse operation. The triple Langmuir probe measured electron density and temperature inside the thruster; during most discharges it was positioned halfway between the electrodes at an axial position 5 cm upstream of the thruster exit plane. During a typical discharge, the electron density

and temperature traces display a structure divided into three phases. At the time of breakdown and for approximately 1–3 ms thereafter, the probe measures little or no plasma near the exit of the thruster even though current flows between the electrodes. The delay between the beginning of the discharge and the appearance of the density pulse at the position of the probe had an approximately linear dependence on the strength of the applied field. For 10 MW discharges in deuterium, the delay was 1.5 ms for an applied field of 100 G, and 3 ms for an applied field of 200 G. After this initial quiescent period, the probe measures a pulse of high electron density. In 10 MW discharges with helium propellant, the density during this pulse was typically $1.5 - 2 \times 10^{14}$ cm^{-3}, and the pulse lasted for approximately 1 ms. Subsequently, the density would drop to a value approximately one-fourth of that measured during the pulse and remained quasi-steady at this lower value for the duration of the discharge.

The dependence of the timing of the density pulse upon the strength of the applied magnetic field indicates that the phenomenon arises as a result of the shape of the unoptimized field. In this unoptimized geometry, the magnetic field at the end of the thruster is approximately radial; thus there are magnetic "lines of force" stretched between the two electrodes. As the discharge strikes in the upstream section of the thruster and begins to move towards the exit plane, the magnetic tension of the field lines at the end of the thruster will tend to trap the plasma in the thruster. As the plasma density and temperature build up in thruster, the current also ramps up until it reaches a level at which the azimuthal magnetic field has a pressure sufficient to overcome the tension of the radial applied field near the thruster exit. The plasma then stretches and diffuses through the resisting applied field and exits the thruster. The 1 ms high density pulse observed by the probe is believed to be the plasma that has built up in the thruster before it "bursts the bubble." Once the plasma breaks through the applied field, the density drops to the quasi-steady value.

F. Time of Flight Velocity Measurement

As described above, the neutral particle time of flight spectrometer consists of a rotating chopper wheel, drift tube, and detector electronics. As the chopper wheel rotates to the transmission position, UV light from the discharge propagates down the drift tube and impinges on the detector. This UV light signal triggers the gating of the high voltage required to detect neutral particles and also is used as a time fiducial (see Fig. 11). The initial signal spike is from the UV light, non-specularly reflected from the Cu-Be detector into the electron multiplier. This serves as both a time fiducial and gating signal for the detection of neutral particles. The remainder of the signal is from neutral particles incident on the Cu-Be plate ejecting secondary electrons. The directed energy of the neutrals is thus determined by the time delay

between the UV fiducial and the neutral particle arrival time. In this particular example the neutral particles demonstrate a distribution which is very narrow in velocity space (nearly mono-energetic distribution) with $v_z \sim 2.3 \times 10^5$ m/s. The detector requires a minimum amount of UV light to trigger the high voltage gate. If the UV light is insufficient to trigger the gate, the high voltage remains off and no particles are detected.

In previous short pulse work, the mass flow rate was largely an unknown quantity. It is suspected that the electrode surfaces then were a major source of working gas during the discharge evidenced by the fact that following a typical shot the thruster could be fired for a successive shot without actuating the gas valve. It was found in the present upgraded thruster configuration that time of flight spectrometer signals were difficult to obtain. When operating with the long pulse gas valve, the UV light signal was usually insufficient to trigger the high voltage gate. In addition, long pulse gas valve operation introduces a large inventory of neutral working gas into the CTX tank. While this neutral gas provides the source of "charge-exchange" neutrals, too large an inventory also provides a thick cloud of scattering centers which acts to attenuate the charge-exchange neutrals. TOF signals were observed that demonstrate both of these effects. Signals were obtained with no UV gating signal, hence no neutrals could be detected even if present. Signals were also observed with UV gating but no subsequent particle signal indicating the lack of source charge-exchange neutrals or the attenuation along the long path to the detector. To obtain a signal, the propellant mass flow rate was reduced from that typically used until the UV signal was sufficient to gate the detector and neutral particles were observed. This caused the thruster to operate in what appeared to be a "gas starved" mode. Thruster impedance and voltage fluctuation levels were increased over those observed in discharges with higher mass flow rate. The time of flight data presented below need to be viewed in this context.

Reduced TOF data are presented in Fig. 12 for 10 MW deuterium and helium CTX discharges. (Argon flow velocities were unobtainable by this method.) Several conclusions can be extracted from these data. Firstly, the deuterium axial velocities are greater than those for helium by roughly the root inverse mass ratio as should be expected (if all other conditions are held constant) from the ideal MHD nozzle theory since the flow is predicted to reach the magnetosonic speed. Secondly, the measured flow velocities are larger in absolute magnitude than those predicted by the theory. One possible explanation is that these *gas starved* discharges are operating at much lower $\dot{M}$ ($v_z \sim I^2/\dot{M}$) than comparable non-degraded discharges. Another possible explanation resides in the ideal MHD theory itself which predicts v_z continually increasing from C_{A0} to $\sqrt{3}C_{A0}$ as the flow is accelerated in the diverging part of the magnetic nozzle. (Here, C_{A0} is the Alfvén speed in an effective nozzle throat, as discussed later below.) This is in good agreement with the observations which show that $v_z/C_{A0} \sim 2.1 \pm 0.5$. Since we cannot uniquely identify the source location

(along the line of sight) for the charge-exchange emission, we should expect to measure a range of velocities from C_{A0} to $\sqrt{3}C_{A0}$ as we have (Fig. 12). Here, one must remember that, due to the long time scales of the discharge compared to earlier CTX work, (C. W. Barnes et al. 1990) the magnetic nozzle formation previously envisioned as a confluence of emerging and returning applied flux, as facilitated by the condition of frozen foot-points, is no longer tenable. However, indirect evidence will be presented later on in this report, to the effect that a nozzle constriction is nevertheless present in the flow field.

Thirdly, the observed neutral temperatures $\gtrsim 100$ ev are in reasonable agreement with predictions based on eventual thermalization of ions accelerated to E/B (i.e. for deuterium at 100eV, $v_z \sim 10^5$ m/s $\sim E/B$). One also needs to remember that the time-average energy of a charged particle along a cusped cycloidic orbit is twice the energy associated with the guiding-center velocity. Moreover, the helium ions would be expected to possess higher thermal energy than deuterium by virtue of their higher mass if accelerated to the same E/B velocity. Finally, the large amount of scatter in this temperature data also may be attributed to our inability to control or identify the location of emission. The ideal MHD theory also predicts that the local temperature should decrease as the flow progress axially, giving up thermal energy in favor of flow energy as the fluid is accelerated in the nozzle channel. We conclude that various competing effects probably contribute to the effective temperature of the neutrals, T_n, observed downstream. This T_n would be difficult to predict quantitatively, but qualitatively it has the expected order of magnitude. Here, it is important to remember that the measured neutral temperatures, presumably due to collisions with ions (including charge-exchange collisions), are obtained under anomalous (gas-starved) conditions and also downstream of the muzzle, so they may not be representative of ion temperatures in the coaxial flow region.

G. Estimates of Thruster Performance

Measurements of plasma density in the muzzle, and concomitant projections of density in the breech (from a Bernoulli flow model) allow preliminary comparisons to be made with the predicted self-field MHD performance. From our previously discussed model of plasma flow in a converging-diverging magnetic nozzle, the plasma flow velocity V_e at the exit of a fully expanded nozzle should be Alfvén like ($V_e \sim \sqrt{3}C_{A0}$) (Schoenberg, et al. 1991, Schoenberg, et al. 1992). Measurements of the axial neutral flow for helium, made with the time-of-flight spectrometer, indicate a mean axial flow velocity of $\sim 1.5 \pm 0.5 \times 10^5$ m/s. In comparison, the estimated self-field Alfvén velocity, based on measurements of thruster current and plasma density in the muzzle during the axial flow velocity measurement, was $C_{A0} \sim 0.8 \pm 0.3 \times 10^5$ m/s. The MHD model predicts a flow velocity for fully accelerated ions downstream of the exit plane of $V_e = \sqrt{3}C_{A0} \sim 1.4 \pm 0.5 \times 10^5$ m/s, (Schoenberg, et al. 1991,

13

Schoenberg, et al. 1992) and is in good agreement with the neutral particle velocity data. The mean flow velocity is observed to remain roughly constant during the quasi-steady-state period of the discharge ($\sim$3 to 12 ms). The basic agreement between the measured flow velocity during quasi-steady-state operation and the self-field MHD model prediction is consistent with previous work (Schoenberg, et al. 1991, Schoenberg, et al. 1992) and suggests that converging-diverging nozzle flow may be an important constituent of gross plasma acceleration in the present CTX thruster.

The measured values of plasma density, temperature, and flow velocity allow an assessment of "plasma quality". Assuming classical resistivity, these values project a magnetic Reynolds number of approximately 200 for the 6 MW helium discharges. This relatively large magnetic Reynolds number is indicative of good coupling between the plasma propellant and the magnetic fields and is consistent with the observed ideal MHD-like thruster performance.

IV. ANALYSIS AND INTERPRETATION OF CTX DISCHARGES NEAR THE 10-MW, 10-ms OPERATING REGIME

A. Introduction

The present report deals with the properties of CTX discharges in applied magnetic fields that intercept both electrodes, as in the previous NASA report on CTX operation (Schoenberg 1993a). (A more detailed version of that report is to be published in a forthcoming issue of *IEEE Transactions on Plasma Science*). However, the present work extends the previous work to discharges of much longer duration and much smaller power levels, so as to increase the relevance of the research to "near-term" electric propulsion of space vehicles.

The longer duration of the present CTX discharges precludes the possibility of magnetic nozzle formation of the kind discussed in the earlier NASA report, and as used to form spheromaks by C. Barnes et al. (1990), because the transverse field lines in this configuration are no longer anchored in the (resistive) electrodes on the discharge time scale. (Other applied magnetic field configurations in CTX, and their associated anode-fall voltages, are presently being investigated in DOE-supported research.) The spatial disposition of these transverse field lines as distorted by the flowing plasma is described in terms of magnetic diagnostics in the section of this report that presents the results of various measurements. The principal hallmark of this distorted magnetic field is the amount of applied magnetic flux expelled from the annular channel of the coaxial plasma accelerator.

In the following subsection (IV.-B), a simple field-line stretching model is invoked to explain the amount of applied flux expelled beyond the muzzle of the accelerator

14

by the plasma. The occurrence of the Hall effect proves to be an essential ingredient of the model. This model provides an heuristic understanding of the amount of flux so expelled. Furthermore, this model provides an independent means of estimating plasma velocity based on the amount of field line displacement observed. Plasma velocities estimated in this manner are in rough agreement with the magnetosonic speed calculated based upon electron temperature and density measurements, and upon ion temperatures inferred as described below in section (IV.-C).

Although the experiments described herein do not clearly present us with a definite nozzle configuration, magnetic or otherwise, the generalized Bernoulli relation can be utilized together with experimental data on voltage V, current I, and mass flow, $\dot{M}$, to infer the presence of a moderate effective constriction of width Δ_0 in the flow channel, as is described in subsection (IV.-C). Such an effective constriction may be formed as the plasma tries to move downstream between the conducting anode on the outside and the stretched applied magnetic field on the inside. (A different possible cause for the formation of such a constriction has been suggested by self-field runs with the Mach-2 simulation code (not presented here), in which some cold gas from the radial injectors is shown to be deposited along the outer wall of the annular channel.) In addition to inferring the presence of a moderate constriction, the above-mentioned approach also simultaneously provides an inference of the flow velocity of ions newly created in the upstream region of the plasma accelerator. It is interesting that this inferred initial velocity has proven to be near the Alfvén critical ionization velocity (CIV) for all gases studied (deuterium, helium, and argon), and also agrees well with the "self-field" (E_r/B_θ) drift velocity in the upstream region.

In the final subsection, (IV.-D), of Analysis and Interpretation, the implications for self-field MHD thrusters dominated by the CIV condition, as was CTX, are discussed. It is thereby concluded that self-field thrusters operated at high currents are conducive to operation at low "electrical effort," defined as $(m_i/e)(I/\dot{M})$. (Such high current operation also is conducive to operation at or near a state of full ionization, according to the viewpoint of Choueiri (E. Y. Choueiri et al., 1985).) Hence, in some sense, these high-current thrusters represent a more benign operating regime than that of low-current operation. (A larger exerted electrical effort signifies that more charge must be transferred across the channel to expel a given amount of mass downstream, which engenders more wear and tear on the electrodes.) Of course, high current operation that maintains a smaller electrical effort also points toward the utilization of thrusters with larger geometric scale that limits the surface power density on the accelerator walls. This feature also is consistent with the identification of the electrical effort as the quantity $(c/\omega_{pi}\Delta)$, the ratio of the ion skin depth to the channel width (Schoenberg 1991). From this relation, it can be shown that a large electrical effort generally is associated with ion orbits that are large compared to the channel width.

By invoking the "ion-entrainment-heating model" (Schoenberg 1993a,b), the above-described inferences from the Bernoulli equation can be extended to provide estimates of the ion orbit sizes compared to the channel width, as will be done in subsection (IV.-C). We finally conclude that, for self-field MHD thrusters dominated by the CIV condition, heavier species are more demanding as regards the high current levels required to limit the electrical effort. Examples are provided.

B. Application of the Field Line Stretching Model

A quantitative analysis of the time-dependent flux profiles shown in Figs. 10a–d is attempted. By looking at the amount of flux which crosses the exit plane of the thruster, we can obtain a rough idea of the axial distance a field line is displaced during a discharge. For example, considering Fig. 10b, one can see that the last field line to cross the exit plane is roughly 4.4 mWb. From computer modeling calculations of the $B_{r,z}$ coil, this flux surface would initially be about 25 cm inside the muzzle of the thruster. Thus, the experimental displacement distance seems to be on the order of tens of centimeters.

A simple one dimensional model of the field line displacement has been developed to account for the observed displacement, based upon the following assumptions:

- The plasma is taken to be a uniform resistive fluid moving axially with constant velocity v_z and possibly a constant rotational velocity v_y. The model is non-self consistent in that the back-reaction of stretched field lines on the plasma is ignored.

- The problem is reduced to slab geometry with the x-coordinate corresponding to the radial direction, the z-coordinate to the axial direction, and the y-coordinate to the azimuthal direction. Neglect of cylindrical effects generally requires that the ratio of the interelectrode spacing to the average channel radius, Δ/r, be much less than 1. In the case of CTX this ratio is roughly 0.43 (10 cm/23 cm), a relatively high value. However, detailed analysis has shown that the correction to cylindrical geometry proves to be a very small effect even with $\Delta/r \sim 0.4$.

- The magnetic field lines are assumed to be pinned at the anode and cathode surfaces. It will be seen from the flux plots that this assumption is not accurately satisfied, at least near the exit plane of the thruster. The resistive electrodes allow the field-line footpoints to move downstream during the discharge. However, the assumption is made as a first approximation in order to allow a basic quantitative analysis to be performed. This analysis should thus provide an underestimate of the axial displacement of applied magnetic flux.

- Local translational symmetry is assumed, so there is no z dependence of any physical observable. This assumption implies a negligible radial current density, which is primarily associated with the self-field; but the presence of the self-field is neglected in this simple model, which merely focuses upon the stretching of the applied field

16

lines due to the axial flow of conducting fluid. The assumption is necessary, more-over, in order to allow the development of a simple one dimensional model. If the radial current and self-field are not neglected, the problem becomes a two dimensional one requiring complicated numerical solutions. The model may be somewhat rationalized by imagining that the plasma has been pre-accelerated in the region upstream of the applied magnetic field, so that the self-field already has been depleted upstream of the applied field.

- Steady state is assumed so all time derivatives vanish. This assumption may not be valid during the first few milliseconds of the discharge when the field lines are undergoing much of their distortion. However, we are considering in this model the quasi-steady state period of the discharge. This analysis allows calculation of the equilibrium field line shape during the quasi- steady state phase of the discharge, in which the tension force within the magnetic field lines exactly balances the resistive stretching force exerted by the flowing plasma.

- Axisymmetry is assumed so all derivatives with respect to the y- coordinate vanish.

When the Hall effect is included, the equation for the shape of a field line then can be expressed as

$$\zeta(\xi) = \left(\frac{B_z}{B_x}\right)_{\text{vac}} (\xi + \frac{1}{2}) - \frac{1}{2}K_z(\xi^2 - \frac{1}{4}) \ ,$$

where $-\frac{1}{2} < \xi < \frac{1}{2}$ and K_z is the effective magnetic Reynolds number:

$$K_z = R_m \frac{1 + \Omega_x(v_y/v_z)}{1 + \Omega_x^2}$$

$$v_y/v_z \approx \frac{E_r \times B_z}{E_r \times B_y} = B_z/B_y$$

$$\Omega_x = \frac{eB_x}{m_e \nu_e}$$

$$\nu_e \ [\text{sec}^{-1}] \approx 2.91 \cdot 10^{-6} n_e \ [\text{cm}^{-3}] \ (\ln \Lambda) \ (T_e \ [\text{eV}] \ )^{-3/2}$$

In these equations describing the magnetic field shape, ξ represents the nondimensional radial position, defined as x/Δ, where Δ is the interelectrode spacing. The variable ζ is the nondimensional axial location of the field line, defined by z/Δ. Here z is taken to be zero at the cathode foot-point of the field line. (R_m is the usual magnetic Reynolds number defined as $(v_z \Delta \mu_0/\eta)$ where η is the resistivity of plasma.) A diagram of this model for field line stretching is shown in Fig. 13. A detailed derivation of the equation for the distorted field line shape, $\zeta(\xi)$, is provided in Appendix C.

The following values correspond to a typical helium shot in the series (279–295)

17

used to obtain the magnetic field measurements.

$$B_x \approx 0.0035\text{T}$$

$$B_y = \frac{\mu_o I}{2\pi r} \approx \frac{(4\pi \cdot 10^{-7})(60000\text{A})}{2\pi(0.23\text{m})} = 0.052\text{T}$$

$$B_z \approx 0.0035\text{T}$$

$$n_e \approx 0.7 \times 10^{14}\text{cm}^{-3}$$

$$\ln\Lambda \approx 10$$

$$T_e \approx 4\text{eV}$$

For this calculation, we shall assume a nominal axial velocity, $V_z = 1.0 \times 10^5$ m/s, which is about midway between the self-field Alfvén speed and the observed time-of-flight velocities of neutral particles observed downstream. Using these values, we obtain the following:

$$\nu_e = 2.6 \cdot 10^8 \text{sec}^{-1}$$

$$\Omega_x = 2.4$$

$$K_z = 17.2$$

The radial position of maximum stretching is given by the equation:

$$\xi_{\text{nose}} = \frac{1}{K_z}\left(\frac{B_z}{B_x}\right)_{\text{vac}} \approx -0.05$$

Therefore, the maximum stretching distance is:

$$\zeta(\xi_{\text{nose}}) \approx 1.7$$

This result corresponds to 17 cm which is fairly close to the experimentally obtained value, 25 cm. As mentioned earlier, it is to be expected that the observed flux displacement in the downstream direction should somewhat exceed the model prediction, since the electrodes are slightly resistive and allow the field-line footpoints to be dragged downstream during the time-scale of a discharge.

Now, we can consider the reverse procedure. Taking the experimentally measured field line displacement, work backward to determine the effective magnetic Reynolds number, and consequently, the plasma velocity. Making the simplifying assumption, $\xi_{\text{crit}} \approx 0$, the equation for $\zeta(\xi_{\text{crit}})$ becomes

$$\zeta(\xi_{\text{nose}}) = \frac{1}{2}\left(\frac{B_z}{B_x}\right)_{\text{vac}} + \frac{1}{8}K_z.$$

Therefore,

$$K_z = -4\left(\frac{B_z}{B_x}\right)_{\text{vac}} + 8\zeta(\xi_{\text{nose}}).$$

18

Letting $\left(\frac{B_z}{B_x}\right)_{\text{vac}} = -1$ and taking the experimental value of ζ as $\frac{25\text{cm}}{10\text{cm}} = 2.5$, the result is

$$K_z = 4 + 8(2.5) = 24 \ ,$$

to be compared with the earlier value of 17. Now, with D the resistive diffusivity defined by $D = \eta/\mu_0$, where η is the plasma resistivity, one has $D \approx 100$ m^2/s with $T_e \approx 4$ ev,

$$K_z = \left(\frac{V\Delta}{D}\right)\left[\frac{1 + \Omega_x(v_y/v_z)}{1 + \Omega_x^2}\right]$$

$$V = \left(\frac{K_z D}{\Delta}\right)\left[\frac{1 + \Omega_x^2}{1 + \Omega_x(v_y/v_z)}\right]$$

$$\approx \frac{(24)(100)}{0.1}\left[\frac{1 + (2.4)^2}{1 + 2.4(\frac{0.0035}{0.052})}\right]$$

$$= 1.4 \cdot 10^5 \text{m/s}$$

Thus, the field-line stretching model, when used in reverse, provides reasonable agreement with the self-field Alfvén speed and the observed axial velocities. For the same reason as mentioned above concerning slightly resistive electrodes, the model prediction of the velocity required to produce the observed flux displacement will be slightly high, because the model foot-points are pinned in perfectly conducting walls. (The thermal correction to the self-field Alfvén speed is $[1 + (\beta/2)]$, and is usually only a 10–15% correction for helium and deuterium as we show later on.)

The current density inside the thruster plume is proportional to the curl of the magnetic field. With axisymmetry, this can be expressed as

$$j_z = \frac{1}{\mu_o r}\frac{\partial}{\partial r}(rB_\theta)$$

$$j_r = -\frac{1}{\mu_o}\frac{\partial B_\theta}{\partial z}$$

Because the magnetic field data was obtained at a finite number of points, a finite difference approximation was used to compute the partial derivatives. Figures 14a-c show radial current density profiles calculated by the above method. The three dimensional plots show radial current on the vertical z-axis, plotted versus radial position on the x-axis and axial position on the z-axis. Figures 15a-c show an axial cross section of the radial current density taken at a radial position 25 cm from the axis of the tank. All of these figures show radial current dropping off rapidly within 10 cm of the exit plane of the thruster. Furthermore, a reversal of the radial current occurs between 10 cm and 15 cm from the exit plane. This current reversal becomes prominent during the quasi-steady portion of the discharge as can be seen in Fig. 15c.

The total radial current outside the thruster can be determined by numerically integrating the radial current density data. At 2 ms, the total radial current outside

19

the thruster is roughly 6.2 kA. The total thruster current at 2 ms during these helium discharges was roughly 60 kA. Therefore, only about 10% of the total radial current flow occurs outside of the thruster at 2 ms into the discharge. The same procedure can be performed on the data at 4 ms and 8 ms. The results at both times show that roughly 16 kA of radial current, or about 27% of the total thruster current occurs in front of the thruster. These results indicate that throughout the discharge, most of the current remains inside the thruster.

C. Inferences of Some Internal Properties of the CTX Discharges

In this section we shall utilize the conservation laws of steady, axisymmetric, ideal MHD flow in a thin (quasi-1D) annular channel of constant average radius, and the model of ion-entrainment-heating described in our previous NASA report, (K. Schoenberg et al., NASA Contractor Report 191084, March 1993) together with experimental data, to infer certain internal properties of the plasma propellant. These properties have not been accessible to direct measurement. The inferred properties are:

- the propellant velocity in the upstream region;

- the presence of an effective nozzle constriction;

- the ion "beta" (ratio of ion thermal pressure to self-field magnetic pressure);

- the ion gyro-radius.

The assumption of self-field channel flow within the accelerator will be made, $B \approx B_\theta$, as motivated, in part, by the observation that the flowing magneto-plasma expels a substantial amount of applied flux from within the channel and, in part, by the usually much smaller B_{rz}^2 values estimated for the applied field as compared with the B_θ^2 self field value. There is other compelling evidence to suggest that the propellant flow is obeying a self-field description within the accelerator, which will be presented shortly below. Moreover, the MHD conservation laws will be utilized only upstream of the presumed "nozzle," wherein B_θ is still comparable to its maximum value.

The assumption of cold flow will be made, $P \ll (B_\theta^2/2\mu_0)$, which is consistent *a posteriori* with the obtained result that the inferred ion beta values often prove to be moderately small compared to unity. Moreover, the smallness of the electron temperatures observed in this set of experiments justifies the neglect of the electron pressure compared with the inferred ion pressure. However, some of the cold-flow model results prove to be exact with respect to thermal effects, within the context of ideal MHD. Moreover, self-consistent thermal effects are taken into account in the Tables presented at the end of this report, by means of the methods presented in Appendix B.

An interesting (but not unprecedented) characteristic of the experiments described herein is their apparent display of the Alfvén CIV phenomenon. Alfvén hypothesized that incident neutral particles falling from afar towards the sun (without appreciable angular momentum) could be stopped away from the sun by ions trapped in an ambient magnetic field, provided that the kinetic energy of the neutrals (in the rest frame of the ions) exceeded the ionization energy of the neutrals. Alfvén hypothesized that this energetically allowed ionization process would then indeed occur, so that the neutrals would become ionized, would become trapped in the ambient magnetic field, and therefore would not fall into the sun. In this way, matter would be able to accrete at some distance from the sun, thereby providing a basis for the formation of the planets. (Neutral particles incident from afar with appreciable angular momentum would remain on untrapped orbits in the absence of prior accretion but could also become trapped by this mechanism.) (See H. Alfvén, 1960, and references therein.) When Alfvén presented this concept, it was at first met with skepticism, but has since enjoyed decades of experimental confirmation, both in the laboratory and in space-physics experiments, covering orders-of-magnitude ranges of the principal parameters. In the laboratory, ions accelerated against resting neutrals appear to have a velocity limit at the CIV as long as the gas is not completely ionized. The laboratory signature of this velocity saturation usually is the (E/B) drift velocity of the ions, as inferred from the proportionality of discharge voltage to the magnetic field strength. The latter usually has been a strong externally applied transverse magnetic field in CIV-oriented experiments. In spite of these striking experimental results, there is as yet no comprehensive, detailed theoretical understanding of how this happens. However, there is general agreement among researchers in this subject that direct collisions between heavy particles cannot, by themselves, account for the observed ionization process; thus, micro-instabilities that populate the high-energy tail of the electron distribution are presently suspected as enabling part of the electron population to achieve the ionization. The entire subject has recently received a thorough review by Brenning (N. Brenning, 1992). Also, Choueiri et al. (op. cit) have studied the CIV process specifically in connection with the characteristics of magneto-plasma-dynamic self-field thrusters.

Let us provisionally suppose that V_{CIV} is indeed the characteristic fluid (i.e., guiding-center) velocity of ions in the breech (upstream) region of the CTX accelerator (where the bulk of the ionization is presumed to occur), and let us identify this velocity with the *self-field* drift velocity, (E_r/B_θ). It follows that, within the quasi-1D thin-channel approximation, which is approximately valid for CTX,

$$V_{\text{CIV}} = \frac{E_r}{B_\theta} = \frac{\mathbf{V}}{\Delta} \frac{2\pi r}{\mu_0 I} \quad,$$

where Δ is the channel width, r is the average channel radius, B_θ in the breech is related by Ampere's law to the total discharge current I, and $\mathbf{V}$ is the discharge

voltage appearing across the channel. Of course, this (E/B) drift scenario for the ions presupposes that the ion gyro-orbits are not frequently disrupted by collisions.

Now, the above relation provides a prescription for the device impedance, namely,

$$R = \frac{\mu_0}{2\pi} V_{CIV} \frac{\Delta}{r} \ .$$

This is the apparent resistance of the discharge.

Measuring V_{CIV} in seconds (like specific impulse), this discharge resistance becomes

$$R[\text{Ohms}] = (V_{CIV} \ [\text{sec}]) \times 10^{-6} \times \left(\frac{2\Delta}{r}\right) [\Omega] \ .$$

In the CTX device, one has $(2\Delta/r) \approx 1$ (which is almost exact if the dominant ionization takes place close to the cathode) so that the discharge resistance can be approximately expressed as

$$R[\text{milliohms}] \approx (V_{CIV} \ [\text{sec}]) \times 10^{-3}[\text{m}\Omega] \ .$$

Since critical ionization velocities generally lie in the range of a few thousand seconds, the above expression implies that the discharge resistance should be in the few-milliohm range (i.e., in the "$\text{m}\Omega$" range).

Approximate values of V_{CIV} that prove to yield good agreement with observed discharge resistances for the propellants corresponding to deuterium, helium, and argon are as follows:

$$
\begin{aligned}
\text{Deuterium } (D_2 \longrightarrow D^+ + D^+) \ &: \ V_{CIV} = 4800 \text{ sec.} \\
&: \qquad\qquad (5500 \text{ sec.}) \\
\text{Helium } (He \longrightarrow He^+) \qquad\quad &: \ V_{CIV} = 3500 \text{ sec.} \\
\text{Argon } (Ar \longrightarrow Ar^{++}) \qquad\quad &: \ V_{CIV} = 1450 \text{ sec.}
\end{aligned}
$$

Here, we are considering the direct double-ionization of argon, rather than a multi-step process, $Ar \longrightarrow Ar^+ \longrightarrow Ar^{++}$. The multi-step process would, at first glance, be unable to utilize the relative velocity of Ar^+ and Ar^{++} within the framework of the CIV process, as they both have the same guiding-center drift velocity; however, there may be non-guiding-center effects which could come into play on short time scales. (The direct double ionization of argon usually is not considered in connection with the CIV process, but is suggested by the discharge impedance in CTX with argon propellant. Additional indirect evidence for Ar^{++} in CTX will be described below.)

Here, it was noted that the center-of-mass energy of colliding particles, such as for $D^+ + D_2 \longrightarrow D^+ + D^+ + D^+$, is not available for ionization; but also that the

time-average energy of an incident ion on a cycloidic orbit that starts at rest is twice the energy of the guiding-center velocity. It is this time-average energy on an individual ion orbit that, at the CIV threshold, is taken to be the ionization (and dissociation) energy plus the center-of-mass energy. Finally, the transition back to the guiding-center velocity is made, and this is what is tabulated above. This particular approach was invoked here as a simple and definite phenomenological procedure. (See J. Sherman, 1968.) If, on the other hand, the guiding-center velocities simply were conventionally taken to have the ionization (and dissociation) energies for the above gases, the V_{CIV} results for helium and argon would be unchanged, and the result for deuterium (in parentheses above) would be only slightly different.

Using the V_{CIV} values listed above, one then computes the following discharge resistances (in mΩ) for the various propellants.

		Calculated	Measured
Deuterium	:	$R \approx 4.8$ mΩ	5.3 ± 0.7 mΩ
	:	(5.5 mΩ)	
Helium	:	$R \approx 3.5$ mΩ	3.4 ± 0.3 mΩ
Argon	:	$R \approx 1.5$ mΩ	1.7 ± 0.05 mΩ

These results present interesting agreement with the experimental results. They thus may constitute evidence that the CIV is operative in the upstream (ionizing) region of the accelerator, probably close to the cathode, and moreover that self-field propellant flow is a good approximation notwithstanding the presence of the transverse applied magnetic field. Apparently, the plasma is able to force a self-field channel flow by laterally and axially displacing the applied magnetic flux.

The conventional picture of nozzle flow is that the high-pressure fluid from a reservoir is accelerated through a nozzle starting almost from rest in the reservoir. However, the above results imply that the ion fluid being accelerated in CTX has already been given an impulsive start in the very process of ion creation. That is, the plasma propellant does not start from rest, but possesses a very substantial initial velocity before it even enters the nozzle region.

This picture of an impulsive start now will be supported by an analysis which uses the conservation laws together with experimental data to "work backwards" and infer properties of the flowing plasma within the accelerator, including the presence of a constriction in the flow. The exact cause and make-up of the constriction remain matters of speculation, however. It may be noted that the detection downstream of axial velocities near to, but somewhat above the self-field Alfvén speed, and substantially above the (E_r/B_θ) drift velocity in the breech of the accelerator, is consistent with the notion of nozzle-like acceleration of the propellant.

23

As a basis for our analysis and interpretation of the 10-MW- 10-ms-class discharges in CTX, we shall first review the conservation laws that will be invoked to infer the internal conditions within the flowing plasma.

Let us suppose that the plasma in a steady, axisymmetric, nonrotating self-field flow, is a perfect electrical conductor,

$$\vec{E} + \vec{V} \times \vec{B} = 0 \quad , \tag{1}$$

and let us suppose also that there is neither mass addition (or loss) nor heat addition (or loss) downstream of the upstream ionization region. Then the total energy balance relation for the plasma and electromagnetic fields can be written as

$$\nabla \cdot \left\{ \vec{V} \left[\frac{1}{2}\rho V^2 + \frac{P}{\gamma - 1} + P \right] + \frac{\vec{E} \times \vec{B}}{\mu_0} \right\} = 0 \quad , \tag{2}$$

wherein ρ is the mass density, $\vec{V}$ is the flow velocity, P is the plasma pressure, $\vec{B}$ is the local magnetic field, and $\vec{E}$ is the local electric field. The Poynting flux is $(\vec{E} \times \vec{B}/\mu_0)$. Here also, γ is the ratio of specific heats, C_p/C_v, which also may be identified with f, the number of degrees of freedom available for particle motion, by $\gamma = [1 + (2/f)]$.

The physical meaning of Eq. (1) is that the magnetic field lines move with the propellant. The physical meaning of Eq. (2) is that the depletion of kinetic and thermal energies and the exertion of pressure-work is compensated by an influx of electromagnetic energy; thus the total energy within a volume is conserved.

The use of Eq. (1) together with local mass conservation,

$$\nabla \cdot (\rho \vec{V}) = 0 \quad , \tag{3}$$

immediately converts Eq. (2) into the following form.

$$\vec{V} \cdot \nabla \left\{ \frac{1}{2}V^2 + \frac{\gamma}{\gamma - 1}\frac{P}{\rho} + \frac{B_\theta^2}{\mu_0 \rho} \right\} = 0 \tag{4}$$

Thus, the "generalized specific enthalpy," namely h given by

$$h \equiv \left\{ \frac{1}{2}V^2 + \frac{\gamma}{\gamma - 1}\frac{P}{\rho} + \frac{B_\theta^2}{\mu_0 \rho} \right\} \quad , \tag{5}$$

is conserved along the flow. The magnetic term can be thought of as arising from the Poynting vector in Eq. (2), written in the form

$$\vec{V} \frac{B_\theta^2}{2\mu_0} + \vec{V} \frac{B_\theta^2}{2\mu_0} \quad ,$$

wherein the first term can be identified with the flow of magnetic energy, and the second term can be identified with the rate of work performed by the magnetic pressure.

Another important conservation law can be derived as a consequence of steady axisymmetry, perfect electrical conductivity, the absence of rotation, and mass conservation, Eq. (3). It reads

$$\frac{B_\theta}{\rho r} = \text{const. along the flow.} \tag{6}$$

Since we consider the case of a thin annular channel of constant average radius, r, Eq. (6) becomes

$$\frac{B_\theta}{\rho} = \text{const. along the flow,} \tag{6-a}$$

when

$$r = \text{const. along the flow.} \tag{6-b}$$

The global form of mass conservation, Eq. (3) in the quasi-1D form

$$\rho V 2\pi r \Delta = \text{const. along the flow,} \tag{7}$$

also proves to be useful. Here, Δ is the width of the annular channel, which may vary along the flow.

Finally, the adiabatic (isentropic) relation should be mentioned, namely

$$P\rho^{-\gamma} = \text{const. along the flow.} \tag{8}$$

Eq. (8) can be derived by the combined utilization of the partial differential equations of ideal MHD governing the local disposition of plasma mass, momentum, and plasma energy.

Now, one can combine the differential forms of Eqs. 5, 6, 7, and 8 to obtain the differential equation that governs the flow of a self-field propellant through an annular nozzle of constant average radius. This equation reads as follows.

$$\left(\frac{V^2}{C_A^2 + C_S^2} - 1 \right) \frac{1}{V}\frac{dV}{dz} = \frac{1}{\Delta}\frac{d\Delta}{dz} \tag{9}$$

(Here, z represents the axial coordinate along the channel.) In this equation, the Alfvén speed is defined by

$$C_A = \sqrt{B_\theta^2/\mu_0 \rho} \tag{10-a}$$

and the speed of sound is defined by

$$C_S = \sqrt{\gamma P/\rho} \; . \tag{10-b}$$

25

The important conclusion to be drawn from the differential equation for annular nozzle flow, Eq. (9), is that continuous acceleration through the throat of the nozzle (at $z = z_0$ where $(d\Delta/dz) = 0$) requires that

$$V^2 = C_A^2 + C_S^2 \quad \text{at } z = z_0 \ .$$
(11

Thus, the flow speed matches the fast-magnetosonic speed in the throat of the self-field annular nozzle.

We shall set $\gamma = 2$ for simplicity. (For hot semi-collisional ions, this value of γ has some physical relevance and, in any case, is not much different from the fully collisional value, $\gamma = 5/3$.) It then follows that the plasma "beta" (the ratio of thermal pressure to magnetic pressure) can be written as

$$\beta = \frac{P}{(B_\theta^2/2\mu_0)} = \frac{(2P/\rho)}{(B_\theta^2/\mu_0\rho)} = \frac{C_S^2}{C_A^2} \ .$$
(12

In view of Eq. (8) with $\gamma = 2$, together with Eq. (6-a), we see that β is conserved along the flow.

We shall find later that β proves to be moderately small. Therefore we shall ignore thermal effects. Then Eq. (5) becomes

$$h = \frac{1}{2}V^2 + C_A^2 = \text{const. along the flow.}$$
(13

Moreover, Eq. (11) now becomes

$$V_0^2 = C_{A0}^2$$
(14

where the subscript "0" means "at the throat of the nozzle." ·

An important relation for the subsequent analysis emerges from applying global, quasi-1D mass conservation, Eq. (7), between the breech (labelled b) and the throat (labelled "0"), and invoking Eqs. 14, 10-a, and 6-a. One has

$$\dot{M} = 2\pi r \Delta_b \rho_b V_b = 2\pi r \Delta_0 \rho_0 V_0 \ ,$$
(15

from which it thus can be shown that

$$\frac{V_b}{C_{Ab}}\frac{\Delta_b}{\Delta_0} = \left(\frac{\rho_0}{\rho_b}\right)^{3/2} \ .$$
(16

Thus, the conservation laws imply a fundamental relationship between the upstream "Alfvén-Mach number," (V_b/C_{Ab}). the nozzle contraction ratio (Δ_b/Δ_0), and the nozzle density ratio, (ρ_0/ρ_b).

Finally, invoking the constancy of h between the breech and the throat, Eq. (13), together with Eqs. (14), (6-a), and (16), one can then reduce Eq. (13) to the relationship

$$\left(\frac{1}{2}\frac{V_b^2}{C_{Ab}^2} + 1\right)^{3/2} = \left(\frac{3}{2}\right)^{3/2}\left(\frac{V_b}{C_{Ab}}\right)\left(\frac{\Delta_b}{\Delta_0}\right) = \left(\frac{3}{2}\frac{\rho_0}{\rho_b}\right)^{3/2} \quad . \tag{17}$$

Thus there is a direct connection between the upstream Alfvén-Mach number and the contraction ratio of the nozzle. This makes sense because, in the "subsonic" region upstream of the throat, the propellant can sense the downstream conditions at the throat. At this point, one can observe that in the limit $V_b^2 \ll C_{Ab}^2$, Eqs. (16) and (17) together imply that

$$\frac{\rho_0}{\rho_b} = \frac{2}{3} \quad (\text{for} \quad V_b^2 \ll C_{Ab}^2) \quad .$$

By defining an upstream energy ratio, ϵ_b, as

$$\epsilon_b \equiv \frac{V_b^2}{C_{Ab}^2} = \frac{\left(\frac{1}{2}\rho_b V_b^2\right)}{\left(\frac{B_{\theta b}^2}{2\mu_0}\right)} \quad , \tag{18}$$

Eq. (17) can be rewritten as

$$A\zeta^3 - \zeta^2 + \frac{1}{2} = 0 \quad , \tag{19}$$

where

$$A \equiv \left(\frac{2}{3}\right)^{3/2}\left(\frac{\Delta_0}{\Delta_b}\right) \tag{20}$$

and

$$\zeta \equiv \sqrt{\frac{1}{\epsilon_b} + \frac{1}{2}} \quad . \tag{21}$$

Equation (19) serves to epitomize the relation between (Δ_0/Δ_b) and (V_b/C_{Ab}), and also the relation with (ρ_0/ρ_b) via Eq. (16). These relations are plotted in Fig. 14. If one has prior knowledge of the contraction ratio from having built the nozzle into the channel walls, then one can solve the cubic equation (19) to obtain the upstream Alfvén-Mach number. In the present set of experiments, such prior knowledge of the contraction ratio does not exist.

The basic ideal MHD machinery has now been laid out. A final step, as a prerequisite for further analysis and interpretation of the experiments (while taking into account the absence of prior knowledge about the contraction ratio), is to develop a direct connection to the experimental measurements, so as to be useful in a quantitative manner. The approach used here is to develop an expression for the discharge resistance using the unknown throat conditions and their ratios to the partly unknown conditions upstream. (It is important to note that the CIV condition is *not* assumed at the outset here.) There then prove to be enough global experimentally measured quantities that several internal unknowns can be inferred, both in the breech and in the throat.

27

By writing the discharge voltage (which is independent of axial position because the electrodes are taken to be perfect conductors) across the throat of a presumed nozzle, throat width Δ_0,

$$\mathbf{V} = E_r \Delta_0 = C_{A0} B_{\theta 0} \Delta_0 \quad,$$

and using the definition of the Alfvén speed (10-a), and conservation law (6-a) between breech and throat, one finds that

$$\mathbf{V} = \Delta_0 x_0^2 \left(\frac{\mu_0 I}{2\pi r}\right)^2 \frac{1}{\sqrt{\mu_0 \rho_0}} \quad. \tag{22}$$

Here, the ubiquitous symbol x_0 is defined as the density ratio,

$$x_0 \equiv (\rho_0/\rho_b) \quad. \tag{23}$$

Then, writing $\dot{M}$ at the throat, $\dot{M} = \rho_0 C_{A0} 2\pi r \Delta_0$, and again using (10-a) and (6-a) between breech and throat, one finds

$$\frac{1}{\sqrt{\mu_0 \rho_0}} = \frac{x_0 I \Delta_0}{\dot{M}} \quad. \tag{24}$$

The use of (24) in (22) yields the discharge resistance as

$$\mathbf{R} \equiv \frac{\mathbf{V}}{I} = \left(\frac{\Delta_0}{r}\right)^2 x_0^3 \left(\frac{\mu_0}{2\pi}\right)^2 \frac{I^2}{\dot{M}} \quad. \tag{25}$$

Now, from Eq. (16), one has

$$x_0^3 = \left(\frac{V_b}{C_{Ab}} \frac{\Delta_b}{\Delta_0}\right)^2 \quad. \tag{26}$$

Using (26) in (25), solving for V_b/C_{Ab}, and converting $\mathbf{R}$ to mΩ, I to kA, and $\dot{M}$ to g/s, one finally has an equation for the upstream Alfvén-Mach number in terms of the experimental data. This equation reads

$$\frac{V_b}{C_{Ab}} = \{\text{Exper.}\} \frac{r}{\Delta_b} \quad, \tag{27}$$

where the experimental data appear in {Exper.} as

$$\{\text{Exper.}\} = \frac{5.0}{I[kA]} \sqrt{\mathbf{R}[\text{m}\Omega] \dot{M}[\text{g/s}]} \quad. \tag{28}$$

Here, it is important to state that Eqs. (27) and (28) that determine (V_b/C_{Ab}) prove to be exact as they stand, within a self-consistent thermal model; see Appendix B. This is because Eq's. (27) and (28) also are directly obtainable from the ideal MHD condition in the breech, $E_{rb} = V_b B_{\theta b}$, without any reference to the conditions at the

28

throat of the nozzle. The exact agreement between the results of the two derivations serves to illustrate the global unity of the quasi-1D, ideal-MHD model of self-field flow in a highly conducting channel. Moreover, Eq. (25) proves directly useful in our subsequent discussion of the significance of $(I^2/\dot{M})$, wherein throat conditions cannot be avoided.

At this point, Eq. (17) can be used to determine the nozzle contraction ratio, (Δ_b/Δ_0). Then Eq. (16) or (26) can be used to determine the density ratio, $x_0 = (\rho_0/\rho_b)$. (These cold-flow results for (Δ_b/Δ_0) and (ρ_0/ρ_b) are subject to thermal corrections; see Appendix B.)

Having inferred the upstream Alfvén-Mach number, (V_b/C_{Ab}), and the nozzle contraction ratio, (Δ_b/Δ_0), we now introduce the ion-entrainment-heating model to allow further inferences. The ion-entrainment-heating model was discussed in detail in our earlier NASA report (K. Schoenberg et al., NASA Contractor Report 191084, March 1993), and deals with the nonideal MHD process of plasma generation in a region upstream of the ideal-MHD flow region. It states that there is equipartition between flow energy and thermal energy in the region of plasma generation.

$$\frac{1}{2}\rho_b V_b^2 = \frac{P_b}{\gamma - 1} \qquad (29\text{-a}$$

With $\gamma = 2$ and dividing through by $C_{Ab}^2 = B_{\theta b}^2/(\mu_0 \rho_b)$, this relation becomes

$$\frac{V_b^2}{C_{Ab}^2} = \frac{P_b}{(B_{\theta b}^2/2\mu_0)} = \beta \quad . \qquad (29\text{-b}$$

Hence, the plasma "beta" is the square of the upstream Alfvén-Mach number, if the ion-entrainment-heating model is valid. (Here, the ion beta, β_i, is to be identified with the plasma beta, β, in view of the small electron temperature in comparison with the inferred ion temperature.)

The ion gyro-radius, r_{ci}, may now be inferred. Introducing the "electrical effort" Ξ as

$$\Xi \equiv \frac{m_i}{e}\frac{I}{\dot{M}} \qquad (30$$

where m_i is the mass of an ion and e is the charge on an electron, one can verify two useful identities.

$$\frac{c}{\omega_{pi} r_{ci}} = \frac{1}{\sqrt{\beta_i}} \qquad (31\text{-a}$$

$$\Xi = \left(\frac{c}{\omega_{pi}\Delta}\right)_b \left(\frac{C_{Ab}}{V_b}\right) \qquad (31\text{-b}$$

In (31-b), c is the speed of light (3×10^8 m/s) and ω_{pi} represents the ion plasma frequency, $\sqrt{(ne^2/\epsilon_0 m_i)}$, where n is the ion number density and ϵ_0 is the electrical permittivity of free space.

From the identities in Eq. (31), and noting Eq. (29-b) for β_i, one finds that the ion gyro-radius can be expressed as

$$\left(\frac{r_{ci}}{\Delta}\right)_b = \Xi\beta_i = \Xi\frac{V_b^2}{C_{Ab}^2} \quad . \tag{32}$$

(It is important to note that Eq. (31-a) is independent of the ion-charge-state, and that ω_{pi} is *defined* as if the charge state were single in Eq. (31-b). Correspondingly, the ion gyro-radius, r_{ci} will be treated as for a single charge, by definition, except where specifically noted.)

From (32) one can note that, since

$$r_{ci} = \frac{v_{thi}}{\omega_{ci}} \tag{33}$$

where v_{thi} is the ion thermal velocity, $\sqrt{2T_i/m_i}$, and ω_{ci} is the ion gyro-frequency, (eB_θ/m_i), and since

$$V_b^2 = v_{thi}^2 \tag{34}$$

according to the ion-entrainment-heating model, (29-a), one can therefore write Eq. (32) in the form

$$\frac{V_b}{C_{Ab}} = \sqrt{\frac{V_b}{\Xi(\omega_{ci}\Delta)_b}} \quad . \tag{35}$$

(Here, as mentioned above, Ξ and ω_{ci} are *defined* for a single charge state.) Since (V_b/C_{Ab}) has already been inferred from ideal MHD and the device parameters, I, $\dot{M}$, R, and (r/Δ_b) and since Ξ, ω_{ci}, and Δ_b are known from experimental measurements of I, $\dot{M}$, and Δ_b, Eq. (35) provides an absolute estimate of V_b. Invoking the ion-entrainment-heating model has enabled this absolute estimate to be possible. We shall find that use of the Alfvén critical ionization velocity for V_b on the right hand side of Eq. (35) nicely reproduces the previously inferred value of V_b/C_{Ab}.

Moreover, continuing in this manner, one can take the previously inferred value of (V_b/C_{Ab}), invoke $V_b = V_{CIV}$, and thereby infer the ion number density in the upstream region. This ought to come out with slightly larger values than n_e measured near the muzzle.

If the CIV condition is indeed operative here, then, according to Eqs. (33) and (34), r_{ci} scales as follows.

$$r_{ci} = \frac{V_{CIV}}{\omega_{ci}} \sim \frac{r}{I}\sqrt{\epsilon_{\text{ioniz.}} m_i}$$

Here, $\epsilon_{\text{ioniz.}}$ represents the energy required to ionize a neutral atom. Clearly, low currents and heavy species will tend to produce large ion orbits, perhaps too large. This point will be discussed later using a different approach.

As examples, we shall now analyze three specific discharges, one for each propellant type used, namely helium, deuterium, and argon. We recall that CTX geometry

has $r = 23$ cm, $\Delta_b = 10$ cm. so that $(r/\Delta_b) = 2.3$. Cold flow as described above is used for simplicity in these three examples, but self-consistent thermal effects are allowed for in Appendix B and in the Tables presented at the end of this paper (including these examples). The number densities quoted at the beginning of each case are n_e measurements, the conditions of which will be specified below.

Case I.—Helium #305

$I = 60$ kA; $\quad$ **V** $= 180$ v; $\quad \dot{M} = 2.25$ g/s;
(**R** $= 3.0$ mΩ); ($\Xi = 1.10$); ($n_e = 0.4 \times 10^{14}$ cm^{-3}; averaging time 5–10 ms;
5 cm upstream of muzzle, 2.5 cm from cathode.)

Applied Field Coil Current = 140 A.

From Eqs. (27) and (28):
Alfvén-Mach number

$$\frac{V_b}{C_{Ab}} = 0.500$$

From Eq. (17):
Nozzle contraction ratio

$$\frac{\Delta_b}{\Delta_0} = 1.30 \quad ; \quad \text{(from Eq. (16): } x_0 = \frac{\rho_0}{\rho_b} = 0.750)$$

From Eq. (29):
Ion beta

$$\beta = 0.250$$

From Eq. (32):
Ion gyro-radius in breech

$$\left(\frac{r_{ci}}{\Delta}\right)_b = 0.275 \quad \text{or} \quad \left(\frac{2r_{ci}}{\Delta}\right)_b = 0.550$$

The Relevance of CIV (a check)

Lastly, we can check again on the relevance of the CIV condition by invoking it on the right-hand side of Eq. (35). Since

$$B_{\theta b} = \frac{\mu_0 I}{2\pi r} = 52.2 \times 10^{-3} \text{ [tesla] },$$

one has, for helium, with $\omega_{ci} = (eB_\theta/m_i)$,

$$(\omega_{ci})_b = \frac{eB_{\theta b}}{m_i} = 1.26 \times 10^6 [\text{s}^{-1}] \quad .$$

31

Then, for $V_b = V_{CIV} = 3500[s] = 35 \times 10^3 [m/s]$, the right-hand side of Eq. (35) becomes

$$\left(\frac{V_{CIV}}{\Xi(\omega_{ci}\Delta)_b} \right)^{1/2} = 0.503 \quad ,$$

in excellent agreement with the upstream Alfvén-Mach number. (The relative error is 6%, and the square has a relative error of 12%, which is the same order as the deviation of shot #305 from Table I as regards the discharge resistance.) Moreover, we can also use the inferred value, $V_b/C_{Ab} = 0.500$ and replace V_b with V_{CIV} for helium, to obtain an estimate of the ion or electron density in the *upstream* region of the accelerator, since C_{Ab} depends upon $(I/r\sqrt{n})$, with $r = 0.23$ m. The result is

$$n_b \approx 0.7 \times 10^{14} \text{ cm}^{-3} \quad ,$$

in reasonable agreement with the measured densities downstream.

This completes our account of Case I.

Case II.—Deuterium #604

$I = 55$ kA; $\quad$ $V = 262$ volts; $\quad$ $\dot{M} = 1.26$ g/s;
($R = 4.76$ mΩ); $\quad$ ($\Xi = 0.903$); $\quad$ ($n_e = 0.78 \times 10^{14}$ cm^{-3}; averaging time 3–10 ms; 5 cm downstream, 5 cm from cathode.)

Applied Field Coil Current = 180 A.

Alfvén-Mach number

$$\frac{V_b}{C_{Ab}} = 0.512$$

Nozzle contraction ratio

$$\frac{\Delta_b}{\Delta_0} = 1.28 \quad ; \quad (x_0 = 0.754)$$

Ion beta

$$\beta = 0.262$$

Ion gyro-radius

$$\left(\frac{r_{ci}}{\Delta} \right)_b = 0.237 \quad \text{or} \quad \left(\frac{2r_{ci}}{\Delta} \right)_b = 0.473$$

The Relevance of CIV (a check)

$$B_{\theta b} = \frac{\mu_0 I}{2\pi r} = 47.8 \times 10^{-3} \text{ [tesla]}$$

32

$$(\omega_{ci})_b = \frac{eB_{\theta b}}{m_i} = 2.31 \times 10^6 [\text{s}^{-1}] \quad .$$

$$V_{\text{CIV}} = 4800[\text{s}] \quad (5500[\text{s}])$$

Eq. (35):

$$\left(\frac{V_{\text{CIV}}}{\Xi(\omega_{ci}\Delta)_b} \right)^{1/2} = 0.480 \quad (0.514)$$

This result is in excellent agreement with the upstream Alfvén-Mach number, especially using the CIV condition according to the guiding-center version of Alfvén's original hypothesis, as opposed to Sherman's interpretation.

Finally, replacing V_b by $V_{\text{CIV}} = 55000$ [m/s] in the above-known ratio (V_b/C_{Ab}), one can estimate the number density of deuterium ions in the upstream region, as $n_b \approx 0.5 \times 10^{14}$ cm^{-3}, which is within about 50% of the measured n_e.

Case III.—Argon #494

$I = 63.4$ kA; $\mathbf{V} = 112$ v; $\dot{M} = 10$ g/s;
($\mathbf{R} = 1.77$ mΩ);   ($\Xi = 2.62$);   ($n_e = 2.6 \times 10^{14}$ cm^{-3}; averaging time 7–13 ms; 5 cm upstream, 5 cm from cathode.)

Applied Field Coil Current = 140 A.

Alfvén-Mach number

$$\frac{V_b}{C_{Ab}} = 0.763$$

Nozzle contraction ratio

$$\frac{\Delta_b}{\Delta_0} = 1.05 \quad ; \quad (x_0 = 0.863)$$

Ion beta

$$\beta = 0.582$$

(The "Cold Flow" model may appear to lose accuracy for argon. However, according to Appendix B, the present result proves to be exact including thermal effects within the ideal-MHD model. Differences with the experimental results, if they were available, would arise from the neglected Hall effect, which is much larger than for the other cases in the case of argon.)

Ion gyro-radius

$$\left(\frac{r_{ci}}{\Delta} \right)_b = 1.52 \quad \text{or} \quad \left(\frac{2r_{ci}}{\Delta} \right)_b = 3.04 \quad (1.52 \quad \text{for} \quad Ar^{++})$$

33

$$B_\theta = \frac{\mu_0 I}{2\pi r} = 5.51 \times 10^{-2} \text{ [tesla]}$$

$$\omega_{ci} = \frac{e B_\theta}{m_i} = 1.33 \times 10^5 [\text{s}^{-1}] \ .$$

$$V_{CIV} = 1450[\text{s}]$$

Eq. (35):

$$\sqrt{\frac{1}{\Xi} \frac{V_{CIV}}{(\omega_{ci}\Delta)_b}} = 0.645$$

This is within $\sim 15\%$ of the value previously inferred for (V_b/C_{Ab}).

Finally, replacing V_b by $V_{CIV} = 14500$ [m/s] (in approximate accord with the measured impedance) in the above-known ratio (V_b/C_{Ab}), one can estimate the number density of argon ions in the upstream region, as $n_b \approx 1.0 \times 10^{14}$ cm^{-3}. For Ar^{++}, this yields the predicted electron density as $n_e = 2n_b \approx 2.0 \times 10^{14}$ cm^{-3}. (Again, the quantitative accuracy may not be very high here because one had to square the (V_b/C_{Ab}) ratio in order to estimate the ion density, and concomitantly because of the neglect of the large Hall effect; see Appendix A.)

Here, one might think that the inference for (Ar^{++}) is not firm, because the inferred n_b scales as $(V_{CIV})^{-2}$, so that for (Ar$^+$), the estimate of 1.0×10^{14} cm^{-3} would, using V_{CIV} for Ar$^+$, be increased up to 3×10^{14} cm^{-3}, which is close to the measured value for n_e, namely 2.6×10^{14} cm^{-3}. However, the use of V_{CIV} for Ar$^+$ in Eq. (35) concomitantly would yield a significantly smaller prediction for (V_b/C_{Ab}), namely ≈ 0.5, which would be in greater disagreement than before with the "experimentally-based" value from ideal MHD, namely 0.76.

Summary of the Results of (IV.-C)

A means of using the global experimental data together with the conservation laws of self-field, cold channel flow in a thin coaxial channel (quasi-1D) has been constructed so as to infer some otherwise inaccessible features of the propellant flow in CTX. (These results also have been extended to include self-consistent thermal effects; see Appendix B and Fig. 14.)

Substantial Alfvén-Mach numbers in the upstream region have been inferred, indicating that the plasma generation process is concomitant with "impulsive start" to the initial flow, which presumably takes place in the upstream ionization layer.

At the same time, moderate nozzle-like constrictions in the flow field have been inferred. (For argon, the inferred constriction with cold flow seems almost negligible, but is larger with the thermal corrections.) However, the origin of the effective nozzle is uncertain. We speculate that it may arise from the distorted applied magnetic flux, but in a manner which must be different from that in the earlier high-power, short-pulse experiments.

By invoking the ion-entrainment-heating model, it becomes possible to further infer values of the ion (plasma) beta, and the ion gyro-radius in the upstream region. For helium and deuterium, the beta-values are moderately small ($\sim$0.25), and the ion gyro-diameters are about half of the channel width. Moreover, these results are meaningful because, for helium and deuterium, it is found that $v_{ii} \ll \omega_{ci}$ for the discharges examined here; that is, when the ion temperature is assumed to be on the order of the ionization (and dissociation) energy according to the CIV model, the ion-ion mean free path for cumulative 90° Coulomb scattering is much larger than r_{ci}. For argon, the beta is substantial ($\sim$0.6), and the gyro-diameter is larger than the channel width. The cold-flow model still has quantitative meaning for estimating the argon beta within ideal MHD (see Appendix B), but the neglected Hall effect can engender some error. The large orbits for argon could indicate that the ions may be carrying a significant part of the discharge current and that there may be substantial wall interaction with the ions. However, for Ar^{++}, this possibility must be tempered by the estimate that, for the considered discharge, $v_{ii} \approx \omega_{ci}$. That is, the ion-ion collisional mean free path is of the same order of magnitude as the size of the gyro-orbit. Even so, the implication is that the Ar^{++} orbits probably will intersect the walls.

Although it is possible in principle to obtain a lower bound for the thruster efficiency, by obtaining the velocity V_o in the nozzle throat from V_{CIV} by means of the ideal MHD conservation laws, and then writing the thruster efficiency as

$$\epsilon > \frac{\frac{1}{2}m_i V_o^2 [volts]}{\Xi V [volts]},$$

such an estimate becomes vulnerable to distortion by small errors in V_o due to the incompleteness of the ideal MHD model. Thus, we have refrained from presenting formal estimates of efficiency. However, we will note qualitatively here, that the observation of time-of-flight deuterium neutrals with energies of $\approx$ 200-300 volts (under anomalous gas-starved conditions), $V \sim 300$ volts, and $\Xi \approx 1$ to 2, is not inconsistent with thrust efficiencies of order 50%. (To realize such an efficiency would require the use of magnetic "trim coils" downstream, to alleviate the detachment process and straighten out the flow. See R. W. Moses et al., 1992).

The presence of the CIV condition is shown, *a posteriori*, to be in good agreement with the previously inferred values of the upstream Alfvén-Mach numbers for helium and deuterium. In the case of argon, the agreement is not as good as for the other

species but is still fairly good. This may be attributed to the deficiency of the ideal-MHD model for argon with respect to the Hall effect. Moreover, the CIV conditions used have been shown earlier above to yield values for the impedances of the discharges that are in good agreement with experiment, within the simple context of self-field flow.

It is interesting to note that the CIV conditions used to obtain this agreement with experiment for the discharge impedances, and to obtain model consistency (with V_b/C_{Ab}), correspond to a CIV process whereby D_2 is "at once" dissociated and fully ionized, and where Ar is "at once" doubly ionized. The latter result suggests that spectroscopic confirmation of the occurrence of Ar^{++} should be attempted in CTX in future work of this kind. Although such direct spectroscopic evidence is not *sufficient* to confirm the direct ionization of Ar^{++} as opposed to a multi-step process, it certainly is a *necessary* consequence of our proposed scenario for argon. But the indirect evidence here for Ar^{++} is three-fold: the discharge impedance; the inference from Eq. (35); and the inference from the predicted vs measured electron density.

D. Characteristics of CIV-Dominated Self-Field MPD Thrusters

In this final subsection of analysis and interpretation, we wish to make the following points. If high-power, coaxial, MHD self-field thrusters are indeed dominated by the Alfvén CIV process in the upstream ionization layer, then certain characteristic features will be present as the CIV signature; and also certain consequences for thruster operation will have to be recognized and dealt with. The basic problem is that the electrical effort parameter is too large when the discharge current is too small. (Here, we use the term "self-field thrusters" in a slightly generalized sense that allows the presence of moderate applied fields or magnetic nozzles that are weak enough to be displaced by a self-field flow.)

First, let us consider certain signatures of the CIV effect. As will be shown in detail shortly, it is found that, for a material nozzle, or for a magnetic nozzle having a controlled contraction ratio due to shape-sensing and feed-back, there then is a close connection between the "initial" velocity, $V_b \equiv V_{CIV}$, and the $(I^2/\dot{M})$ parameter. (This $(I^2/\dot{M})$ parameter usually is identified with the propellant exit velocity, V_{ex}, since $\dot{M}V_{ex}$ is the thrust, which depends only on I^2 for a given self-field thruster.) That is,

$$\frac{I^2}{\dot{M}} \approx \text{const.} \tag{36}$$

for CIV-dominated operation with a given propellant. Therefore, the voltage across the accelerator, calculated at the breech, scales as follows,

$$\mathbf{V} \sim (E_r)_b \sim V_{CIV}(B_\theta)_b \sim \frac{I^2}{\dot{M}}I \ , \tag{37}$$

36

since $E_r = V_z B_\theta$ in ideal MHD, and since $B_{\theta b} = \mu_0 I / 2\pi r$ from Ampere's law.

Thus, the voltage, which generally scales as $I^3/\dot{M}$ for propellants driven by magnetic pressure rather than thermal pressure, finally scales simply with the current during CIV-dominated operation.

$$\mathbf{V} \sim I \tag{38}$$

One has a linear $(I, \mathbf{V})$ characteristic, and a characteristic discharge resistance, as discussed above for CTX. The linearity of the $(I, \mathbf{V})$ characteristic, below a characteristic current level, has been noted experimentally and discussed theoretically in connection with the CIV process by E. Y. Choueiri et al. (op. cit.). This behavior also has been observed in other nozzle-shaped, coaxial plasma-accelerator experiments, for example as noted below.

Another characteristic of CIV-dominated operation follows from the condition at the throat.

$$\frac{I^2}{\dot{M}} \sim C_{A0} \tag{39}$$

This also will be derived below. (Again, we are assuming for simplicity that "cold-flow" constitutes a fairly good approximation.)

From the constancy of $(I^2/\dot{M})$, and noting that $C_{A0} = B_{\theta 0}/\sqrt{\mu_0 n_0 m_i}$, Eq. (39) thus implies that the local plasma number density scales as

$$n \sim B_\theta^2 \sim I^2 \sim \dot{M} \quad . \tag{40}$$

The scalings in Eqs. (38) and (40) have been especially prominent in the detailed experimental observations of recent Russian plasma accelerator research with an annular material nozzle (V. Afanas'ev et al., 1991). However, these researchers did not make the connection of such signatures with the Alfvén CIV phenomenon. (It also should be remarked that such scalings can arise from the finite-beta-limits that are associated with the onset of certain MHD instabilities of the Raleigh-Taylor type, but we cannot dwell on that subject in this report.)

At this point, having described the signatures exhibited by CIV-initiated, self-field, coaxial MHD thrusters with built-in annular nozzles, we shall turn to the practical implications of such thruster operation. From Eq. (25), noting also that $\mathbf{V} = E_r \Delta_b = V_{\text{CIV}} B_{\theta b} \Delta_b$, and $B_{\theta b} = (\mu_0 I)/2\pi r$, one finds that (with $x_0 = \rho_0/\rho_b$)

$$\frac{I^2}{\dot{M}} \left[\frac{\text{kA}^2\text{-s}}{\text{g}} \right] = \frac{1}{20} V_{\text{CIV}} \ [\text{s}] \ \left(\frac{\Delta_b r}{\Delta_0^2} \right) \frac{1}{x_0^3} \quad . \tag{41}$$

This equation (which was referred to above) demonstrates that, for a given geometry, the $(I^2/\dot{M})$ parameter is directly scaled by V_{CIV}, because x_0^3 depends on the geometry via Eqs. (16) and (17). This equation also is of interest in itself, for it makes clear that the ~ 1000 [kA^2-s/g] observed in CTX for helium and deuterium

is not surprising for parameter values $V_{CIV} \approx$ several thousand seconds, $\Delta_b \approx \Delta_0$, $r \approx 2\Delta_0$, and $x_0^3 \approx 1/3$ to $1/2$ as estimated earlier. Finally, in justification of Eq. (39), it is important to note that the ratio (V_0/V_b) also depends only on the geometry, which follows from the invariance of $\dot{M}$.

However, the important point that we now wish to make involves the electrical effort, Ξ. This thruster characteristic is a measure of how hard the thruster must work electrically in order to expel a given amount of mass downstream, Eq. (30). It also is related to the size of the ion gyro-orbit compared to the channel width, Eq. (32).

$$\left(\frac{2r_{ci}}{\Delta}\right)_b = (\Xi)(2\beta_i)$$

Thus, large values of Ξ may not be conducive to radially confined ions. Moreover, Ξ may constitute an important limitation of thruster efficiency. That is because the thruster efficiency (thrust power/input power) can be expressed as (exhaust energy per ion [volts])/(electrical effort $\times$ discharge voltage).

For all of these reasons, it would appear that large values of Ξ ($\Xi \gg 1$) may not be associated with efficient thruster performance and long electrode life. Therefore, we now ask the question as to what operational conditions will insure that Ξ remains a moderate value, $\Xi \lesssim 1$.

This question can be addressed by writing Ξ as follows.

$$\Xi = \frac{m_i}{e}\frac{I}{\dot{M}} = \frac{m_i}{e}\frac{I^2}{\dot{M}}\frac{1}{I} \ ,$$

or

$$\Xi = 10^6 \frac{m_i}{e}\left(\frac{I^2}{\dot{M}}\left[\frac{\text{kA}^2\text{-s}}{\text{g}}\right]\right)\frac{1}{I[\text{kA}]} \ . \tag{42}$$

The utilization of Eq. (41) then yields

$$\Xi = \frac{m_i}{e}\frac{10^9}{I[\text{kA}]}\left\{\frac{V_{CIV}[\text{s}]}{1000}\frac{\Delta_b r}{\Delta_0^2}\frac{1}{20x_0^3}\right\} \ ,$$

or

$$\Xi \approx \frac{1}{2}\frac{\text{A}}{I[\text{kA}]}\left\{\frac{V_{CIV}[\text{s}]}{1000}\frac{\Delta_b r}{\Delta_0^2}\frac{1}{x_0^3}\right\} \ . \tag{43}$$

Here, A is the atomic mass number of the propellant.

For moderate ratios between the breech and the throat, $x_0^3 \approx 1/2$, say, Eq. (43) assumes the following form for deuterium ($\text{A} = 2$). (Here, we take $\Delta_b \approx \Delta_0$ and $r \approx 2\Delta_0$ as in CTX.)

$$\Xi \approx \frac{20}{I[\text{kA}]} \quad \text{(deuterium in CTX)}$$

38

For argon ($\mathbf{A} = 40$), Eq. (45) becomes

$$\Xi \approx \frac{80}{I[\text{kA}]} \quad \text{(argon in CTX)}.$$

(These numbers are slightly underestimated in CTX, since $\Delta_b > \Delta_0$, $r > 2\Delta_0$, and $x_0^3 < 1/2$.) These results indicate that high-current operation may be required to limit the values of Ξ, especially in operation with heavier species.

In connection with these current levels, and to provide a perspective, it is interesting to return to the three examples considered above, in subsection (IV.-C). Using Choueiri's (op. cit.) formula for the characteristic current at full ionization, one finds for helium #305, 40 kA vs 60 kA actual; for deuterium #604, 37 kA vs 55 kA actual; for argon #494, 55 kA vs 63 kA actual. (The much lower J_{fi} currents in Choueiri's argon experiments are explainable by the difference in the ionization energies, by the large disparities in $\dot{M}$, and in geometry, as compared to CTX.) Thus, the CTX experiments described herein are being operated at current levels near to, but somewhat exceeding, Choueiri's estimate of the current level required for full ionization.

In their 1985 paper (op. cit), Choueiri et al. derive a formula for the electric current of a self-field discharge that just achieves full ionization, J_{fi}. They do this by equating two different expressions for the thrust. The first is thrust expressed as the self-field magnetic pressure exerted in the upstream direction on an effective annular area in the breech end of the plasma accelerator. The second is thrust expressed as $\dot{M}V_z$, the rate of propellant momentum emission downstream at the muzzle end of the accelerator, assuming that the mass flow $\dot{M}$ is (almost) fully ionized and that the exit velocity is limited by V_{CIV}. Thus, the assumptions are that there is no nozzle-produced acceleration within the thruster and that the axial velocity V_z now is marginally limited to V_{CIV} (in accord with Alfvén's hypothesis) by the presence of some remnant neutrals (at rest) throughout the accelerator. In the paper of Choueiri et al., the current-voltage characteristics for argon, xenon, and krypton exhibit a linear portion at low currents, consistent with the presence of a characteristic velocity of propellant, followed by a more complex transition to nonlinear characteristics at higher currents. In that paper, the transition point apparently agrees well with the theoretical model-prediction for J_{fi}, notably with the involvement of merely single ionization; e.g., Ar^+. However, it should be kept in mind that the model formula for J_{fi} depends only on the ($\frac{1}{4}$) power of the ionization energy; and moreover that the model's **effective** annular area, which allows magnetic pressure to push in the upstream direction against a metallic structure is, a priori, not a well-known quantity in the Princeton experiments. (In CTX, there is a well-defined metallic annular area in the breech end of the device.)

Thus, it is conceivable that the current at full ionization may sometimes be somewhat larger than the expression given for J_{fi} in the paper of Choueiri et al. Such

an enlargement of J_{fi} might result not only from the occurence of higher ionization states, but also from the possibility that the ion velocity at the muzzle might sometimes exceed V_{CIV} due to nozzling effects. Such nozzle-induced acceleration is not absolutely precluded by the existence of the CIV process because ion-neutral elastic and charge-exchange collisions can act so as to produce some average velocity of neutrals in the downstream direction, as well as to decrease the average velocity of ions in the downstream direction. If so, the **relative** average velocity of ions and neutrals could be reduced below V_{CIV}, thereby introducing the possibility of some nozzle-induced acceleration of the ions. (If the nozzle were a material nozzle as opposed to a magnetic nozzle, then even the neutrals could be so accelerated along with the ions.) We speculate that effects such as these might account for CTX discharge currents that are observed to be moderately above the predicted J_{fi}, notwithstanding that the discharge impedance usually corresponds approximately to ion drift velocities near V_{CIV} in the breech region (or upstream ionization region) of the plasma accelerator.

In conclusion, high-power self-field coaxial thruster operation shows symptoms of the Alfvén CIV phenomenon, both in CTX and elsewhere. In order to maintain a smaller electrical effort, thus inducing better thruster efficiency and reduced ion interaction with the electrodes, high current operation is beneficial. [†] For example, the current should exceed 30 kA in deuterium and 100 kA in argon. In CTX, such a high-current condition was not fulfilled for argon, and Ξ was substantially larger than unity. Coupling this "efficient" high-current operation with near-term space power systems like solar thus necessitates pulsed operation as discussed by Myers et. al.

---

† These statements about reduced electrical effort at high currents are made assuming that the constraint is effectively enforced that $\dot{M}$ scales appropriately with I^2. In this regard, the experiments are generally performed with trial runs with various values of $\dot{M}$ (given I), or various values of I (given $\dot{M}$), to scope-out the "best" discharges. Although there has been no *a priori* selection of device parameters to provide specifically for the constancy of $(I^2/\dot{M})$, the CTX discharges generally are operated at parameter values that are conducive to viable initial electrical breakdown of the working gas at moderate power levels (~ 10 MW range) and at the smallest values of applied flux that allow such electrical breakdowns. Repeatability of the discharges also is a factor in the selection of device parameters. Apparently, this practical approach to device operation leads to the approximate constancy of $(I^2/\dot{M})$, for reasons that are not understood in detail. The Alfvén CIV condition was not even noticed until the data analysis began, long after the experiments had been performed. Moreover, $(I^2/\dot{M})$ may not be perfectly constant in CTX because CTX has no fixed nozzle geometry, contrary to the basic assumption in this section. In fact, there is some limited evidence that the inferred nozzle contraction ratio decreases to a weaker nozzle for larger $\dot{M}$ at fixed I, which may indicate the response of the applied magnetic flux to the altered plasma conditions. Samples of the spread in the CTX data and in the inferences therefrom are indicated in Tables II–IV, in which the inferred results were calculated with account of self-consistent thermal effects according to Appendix B.

V. SUMMARY AND FUTURE WORK

The CTX thruster facility has been upgraded to enable quasi-steady operation over a wide range of power levels (2 to 40 MW). Initial results show time-average quasi-steady operation demonstrated by thruster current, voltage, plasma density, electron temperature, and magnetic field measurements. Furthermore, the long-pulse thruster shows ideal-MHD-like performance similar to that observed during previous short pulse research.

Inferences from the data indicate an impulsive start in the initial propellant flow, presumably in an upstream ionization layer, and the presence of a moderate effective constriction (nozzle) of unknown origin in the flow channel. The initial flow velocities appear to be consistent with the critical ionization velocities, V_{CIV}, for each type of gas utilized in these experiments. (However, the suggestion made here that Ar^{++} is involved in the CIV process in CTX appears to be different than the earlier work of others in which only Ar^+ was thought to be involved.) It was argued that CIV-dominated self-field thrusters may perform better at higher current levels. For near-term space propulsion applications, this conclusion clearly motivates the coupling of high-pulsed-power MPD thrusters with low-mean-power solar sources as discussed by Myers et. al. Hence, the research reported herein supports the expectation that nozzle-based coaxial plasma thrusters can achieve the demanding performance requirements of primary electric propulsion applications.

The experiments on the CTX configurations described herein are not easily amenable to a rigorous quantitative analysis, nor is the interpretation of the present results obvious and clear cut. The simple models employed in our attempts at interpretation must therefore be viewed as provisional, trial models. Some of the difficulties in trying to understand the behavior of CTX originate in the circumstance that the anode fall voltage often is not merely a small fraction of the terminal voltage, and its mitigation by the transverse applied flux has the concomitant effect of partially shorting-out the desired self-field voltage drop across the body of the plasma. Our future research will be focused upon improved magnetic topologies that will better preserve the self-field voltage drop, while offering the potential benefits accrued from more well-defined, axisymmetric, annular magnetic nozzles; such benefits as the mitigation of electrode fall voltages, smoothly distributed plasma acceleration and discharge-current density, and the minimization of velocity losses incurred by the plasma in the detachment process.

Future work will focus on thrust performance measurements (Schoenberg et al. 1992), electrode calorimetry, plume enthalpy, and anode-fall measurements. Detailed maps of plasma parameters (density, temperature, floating potential and flow velocity) and magnetic field fluctuations will be produced for regions both inside and outside of the thruster to uncover optimized magnetic nozzle configurations.

Acknowledgments

References

Afanas'ev, V.P., I. O. Blinov, D.A. Drichko, G.A. Dyuzhev, M.A. Zhakov, D.A. Orlov, and S.V. Kas'yanenko 1991 "Coaxial Plasma Injector in Quasi-steady Operation. I. Plasma Flare," *Sov. Phys. Tech. Phys.* **36** 505.

Afanas'ev, V.P., I.O. Blinov, D.A. Drichko, G.A. Dyuzhev, M.A. Zhakov, D.A. Orlov, and S.V. Kas'yanenko 1991 "Coaxial Plasma Injector in Quasi-steady Operation. II. Plasma Inside the Injector," *Sov. Phys. Tech. Phys.* **36** 511.

Alfvén, H. 1960 "Collision between a Non-Ionized Gas and a Magnetized Plasma," *Rev. Mod. Phys.* **32** 710.

Barnes, C.W., T.R. Jarboe, G.J. Marklin, S.O. Knox, and I. Henins 1990 "Impedance and Energy Efficiency of a Coaxial Magnetized Plasma Source for Spheromak Formation and Sustainment," *Phys. Fluids B* **2** 1871.

Brenning, N. 1992 "Review of the CIV Phenomenon," *Space Science Reviews* **59** 209.

Chen, F.F. 1965 in *Plasma Diagnostic Techniques*, edited by R.H. Huddlestone and S. L. Leonard (Academic, New York).

Choueiri, E.Y., A.J. Kelly, and R.G. Jahn; "The Manifestation of Alfvén's Hypothesis of Critical Ionization Velocity in the Performance of MPD Thrusters;" AIAA-85-2037; presented at the 18th International Electric Propulsion Conference (1985), Alexandria, VA.

Gerwin, R.A., G.J. Marklin, A.G. Sgro, and A.H. Glasser 1990 "Characterization of Plasma Flow Through Magnetic Nozzles," AFOSR Report AL-TR-89-092.

Mayo, R.M., J.C. Fernandez, I. Henins, L.S. Kirschenbaum, C.P. Munson, and F.J. Wysocki 1991 "Time-of-Flight Measurement of Ion Temperature in Spheromaks," *Nuclear Fusion* **31** 2087.

Morozov A. I., and L. S. Solov'ev 1980 "Steady State Plasma Flow in a Magnetic Field," *Reviews of Plasma Physics*, Vol. 8, (Consultants Bureau, New York).

Moses, R.W., R.A. Gerwin, and K.F. Schoenberg 1992 "Resistive Plasma Detachment in Nozzle Based Coaxial Thrusters," in Proceedings of 9th Symposium on Space Nuclear Power Systems CONF-920104, M.S. El-Genk and M.D. Hoover, eds., American Institute of Physics, New York.

Myers, R.M., M. Domonkos, J.H. Gilland. 1993 "Low Power Pulsed MPD Thruster System Analysis and Applications," AIAA 93-2391.

Schoenberg, K.F., R.A. Gerwin, C.W. Barnes, I. Henins, R.M. Mayo, R. Scarberry, and G.A. Wurden 1991 "Coaxial Plasma Thrusters for High Specific Impulse Propulsion," Technical Report AIAA 91-3770, American Institute of Aeronautics and Astronautics.

Schoenberg K.F., R.A. Gerwin, I. Henins, R.M. Mayo, J.T. Scheuer, and G.A. Wurden 1993a "Preliminary Investigation of Power Flow and Electrode Phenomena in a Multi-Megawatt Coaxial Plasma Thruster," NASA Contractor Report 191084, March, 1993.

Schoenberg, K.F., R.A. Gerwin, I. Henins, R.M. Mayo, J.T. Scheuer, and G.A. Wurden 1993b "Preliminary Investigation of Power Flow and Performance Phenomena in a Multi-Megawatt Coaxial Plasma Thruster," Technical Report LA-UR-92-2988, Los Alamos National Laboratory, accepted for publication by *IEEE Trans. Plasma Sci.*, December 1993.

Sherman, J.C. 1968 "Alfvén's Critical Velocity Hypothesis," *Nature* **217** 341.

Sherman, J.C. 1973 "Review of the Critical Velocity of Gas-Plasma Interaction II: Theory," *Astrophys. and Space Science* **24** 487.

Tilley, D.L., A.J. Kelly, and R.G. Jahn 1990 "The Application of the Triple Probe Method to MPD Thruster Plumes," Technical Report AIAA 90-2667.

Voss, D.E., and S.A. Cohen 1982 *Rev. Sci. Instrum.* **53** 1696.

APPENDIX A

THE HALL EFFECT

In the research reported herein, an interesting experimental observation has been that the electrical effort parameter, Ξ, defined as

$$\Xi = \frac{m_i}{e} \frac{I}{\dot{M}} \qquad \text{(A-1}$$

proves to be of order unity. Here, m_i is the mass of an ion, e is the electron charge, I is the discharge current, and $\dot{M}$ is the mass-flow rate. This result implies that the Hall term in Ohm's law may be somewhat comparable to the ideal-MHD term in Ohm's law. Therefore, it becomes important to ascertain whether ideal MHD still retains some approximate quantitative validity for the cases studied here. That is the purpose of this Appendix.

The radial and longitudinal components of the nonresistive Ohm's law for self-field coaxial channel flow now will be written down in slightly generalized "cylindrical" coordinates, wherein "z" signifies the longitudinal coordinate along an ion-fluid streamline, θ is the usual azimuthal angle, and the "radial" coordinate, x, is measured along curves tangent to the local unit vector $\hat{x} = \hat{\theta} \times \hat{z}$. In a quasi-1D sense, the domain of z is approximately the active length of the channel, and the domain of x is approximately the local channel width. Then, the components of Ohm's law read as follows.

$$E_x - V_z B_\theta = -\frac{1}{ne} J_z B_\theta \qquad \text{(A-2--a)}$$

$$E_z = \frac{1}{ne} J_x B_\theta \qquad \text{(A-2--b)}$$

(Here, $\vec{E}$ is the electric field, $\vec{B}$ is the magnetic field, $\vec{J}$ is the current density, n is the electron or ion number density, and $\vec{V}$ is the ion fluid velocity.) The Hall terms appear on the right-hand side of these equations. The electron pressure contribution is ignored as motivated by the experimental observations of low electron temperatures.

In this paper we have repeatedly utilized the radial component of Ohm's law, Eq. (A-2-a), without the Hall term, which is the ideal-MHD version. Therefore, we wish to compare $|J_z/ne|$ to V_z. Information about this comparison can be obtained from the ion-fluid equation of motion,

$$\frac{m_i}{e} \vec{V} \cdot \nabla \vec{V} + \frac{1}{ne} \nabla P_i = \vec{E} + \vec{V} \times \vec{B} \ . \qquad \text{(A-3}$$

(Here P_i represents the ion pressure.)

We provisionally assume that the ion fluid velocity is close to the drift velocity $\vec{V}_E$ as given by

$$\vec{V}_E = \frac{\vec{E} \times \vec{B}}{B^2} \quad . \tag{A-4}$$

Then, the deviation of $\vec{V}$ from $\vec{V}_E$ can be found iteratively as

$$\vec{V} - \vec{V}_E = \frac{m_i}{e} \frac{\vec{B}}{B^2} \times (\vec{V}_E \cdot \nabla \vec{V}_E) + \frac{\vec{B}}{neB^2} \times \nabla P_i \quad . \tag{A-5}$$

(Here, $\vec{B} = B_\theta \hat{\theta}$, since the discussion is restricted to self-field flow.) Then, the longitudinal component of (A-5) reads

$$\frac{V_z - V_{Ez}}{V_{Ez}} = -\frac{m_i}{eB_\theta} \left(\frac{\partial}{\partial z} + \frac{V_{Ex}}{V_{Ez}} \frac{\partial}{\partial x} \right) V_{Ex} - \frac{1}{neB_\theta V_{Ez}} \frac{\partial}{\partial x} P_i \quad . \tag{A-6}$$

The ratio (V_{Ex}/V_{Ez}) can be obtained from Eqs. (A-2), and, to dominant order is given by

$$\left| \frac{V_{Ex}}{V_{Ez}} \right| = \left| \frac{J_x}{neV_z} \right| \approx \Xi \frac{\Delta}{\Delta_z} \quad , \tag{A-7}$$

where Δ is the channel width and Δ_z is the active length of the electrical discharge.

Then, approximating $|\partial P_i / \partial x|$ by (P_i/Δ), introducing β_i through $P_i = \beta_i (B_\theta^2/2\mu_0)$, approximating $|\partial V_{Ex}/\partial x|$ by (V_{Ex}/Δ), assuming to dominant order that $V_{Ez} \approx C_A$, and noting that $C_A/\omega_{ci} = c/\omega_{pi}$, where

$$C_A = \sqrt{B_\theta^2/\mu_0 n m_i}$$

and

$$\omega_{pi} = \sqrt{ne^2/\epsilon_0 m_i} \quad ,$$

Eq. (A-6) can be reduced to the estimate

$$\left| \frac{V_z - V_{Ez}}{V_{Ez}} \right| \equiv \left| \frac{J_z}{neV_{Ez}} \right| \approx \left(\frac{c}{\omega_{pi}\Delta} \right) \left[\frac{\Delta}{\Delta_z} + \Xi \frac{\Delta}{\Delta_z} \right] \left(\Xi \frac{\Delta}{\Delta_z} \right) + \frac{1}{2} \Xi \beta_i \quad . \tag{A-8}$$

Then, noting that $\Xi = (c/\omega_{pi}\Delta)$, Eq. (A-8) finally becomes

$$\left| \frac{J_z}{neV_{Ez}} \right| \approx \left(\Xi \frac{\Delta}{\Delta_z} \right)^2 (1 + \Xi) + \frac{1}{2} \Xi \beta_i \quad . \tag{A-9}$$

The signs of the transverse gradients have been chosen conservatively here, so as not to underestimate the relative magnitude of the Hall effect. However, it is conceivable that one or both of the plus signs in (A-9) could really be minus signs, thereby substantially reducing the relative size of the Hall effect. It also is conceivable that

the strengths of the radial gradients in the bulk plasma have been overestimated in going from Eq. (A-6) to Eq. (A-9). If so, Eq. (A-9) represents an overestimate of the Hall effect compared to ideal MHD.

Thus, if Ξ and β_i were really both small, then we would conclude that the relative importance of the Hall effect is merely second order in the radial component of Ohm's law, thereby providing a justification for ideal MHD. However, we have earlier found Ξ to be of order unity in the CTX experiments. Therefore, the justification of the ideal MHD model for these experiments must rest upon the smallness of β_i, and upon the discharge length being somewhat larger than the channel width. (Equation (A-9) is valid for quasi-neutral plasmas. In principle, there is an additional contribution to J_z from the flow of net charge, but this contribution proves to be very much smaller, of order (V_z^2/c^2).)

For completeness, we now go on to consider the effects of the Hall term upon the conservation laws for $(B_\theta/r\rho)$, and for the generalized specific enthalpy, h.

If one uses the Ohm's law in the form

$$\vec{E} + \vec{u} \times \vec{B} = 0 \quad , \tag{A-10}$$

where $\vec{u}$ represents the electron-fluid velocity (thus exactly including the Hall effect), together with the continuity equation for the electrons, then one can arrive at the result

$$\vec{u} \cdot \nabla \left(\frac{B_\theta}{r n_e} \right) = 0 \quad , \tag{A-11}$$

(where n_e is the electron number density) using the same methods that produced Eq. (6),

$$\vec{V} \cdot \nabla \left(\frac{B_\theta}{r\rho} \right) = 0 \quad .$$

Equation (A-11) represents the constancy of $(B_\theta/r n_e)$ along the electron streamlines. Since the plasmas of interest here are quasi-neutral, one can replace n_e by n or by ρ in Eq. (A-11), and then write that equation as

$$\frac{\vec{V}}{V} \cdot \nabla \left(\frac{B_\theta}{r\rho} \right) = \frac{\vec{J}}{neV} \cdot \nabla \left(\frac{B_\theta}{r\rho} \right) \quad , \tag{A-12}$$

where $\vec{J} = ne(\vec{V} - \vec{u})$. Thus, $(B_\theta/r\rho)$ is not quite constant along an ion streamline. Eq. (A-12) can be written schematically in the "generalized cylindrical coordinates" as

$$\frac{\partial f}{\partial z} - \epsilon'_H \frac{\partial f}{\partial x} = 0 \tag{A-13}$$

where the "small" Hall parameter ϵ'_H is, to leading order, (see Eq. (A-7))

$$\epsilon'_H \equiv \frac{|J_x|}{|neV - J_z|} \approx \Xi \frac{\Delta}{\Delta_z} \quad , \tag{A-14}$$

46

and where f is given by

$$f = \left(\frac{B_\theta}{r\rho}\right) \quad . \tag{A-15}$$

The solution of (A-13) is

$$f = f(\epsilon'_H z + x)$$

Thus, for $\epsilon'_H \ll 1$, one can move large distances along z, say δz, for fixed x (moving along a streamline) and thereby induce only minor variations in f. The relative error so incurred can be displayed as

$$1 + (\epsilon'_H)(\delta z)\frac{f'(x)}{f(x)} \quad ,$$

where $f'(x) = (df/dx)$. Thus, if $\epsilon'_H \ll 1$, the relative error incurred by moving longitudinal distances δz will be negligible. Even if ϵ'_H is not very small, the relative error in the constancy of f can still be small provided that f does not vary much across streamlines, i.e., $|(\delta z)f'(x)| \ll |f(x)|$. The latter condition is especially consonant with the quasi-1D model, wherein the bulk plasma properties (away from wall boundary layers) are envisioned as being practically free of steep radial gradients.

Let us now finally reconsider the constancy along a plasma (or fluid-ion) streamline of the generalized specific enthalpy h, with account of the Hall effect. As before, we begin by writing down the conservation of total energy in the plasma, in the form

$$\nabla \cdot \left\{ \vec{V}\left[\frac{1}{2}\rho V^2 + \frac{\gamma}{\gamma-1}P\right] + \frac{\vec{E} \times \vec{B}}{\mu_0} \right\} = 0 \quad . \tag{A-17}$$

Here, the electron contribution to flow-kinetic energy is neglected because of the small electron mass, and the electron contribution to plasma thermal pressure is neglected because of the low electron temperature. Noting Eq. (A-10), one writes

$$\vec{E} \times \vec{B} = B_\theta^2 \vec{u} = B_\theta^2 \vec{V} - B_\theta^2 \frac{\vec{J}}{ne} \quad . \tag{A-18}$$

Hence (A-17) becomes

$$\nabla \cdot \left\{ (\rho\vec{V})\left[\frac{1}{2}V^2 + \frac{\gamma}{\gamma-1}\frac{P}{\rho} + \frac{B_\theta^2}{\mu_0\rho}\right] \right\} = \nabla \cdot \left(\frac{B_\theta^2}{\mu_0}\frac{\vec{J}}{ne}\right) \quad .$$

Since $\nabla \cdot (\rho\vec{V}) = 0$ downstream of the ionization layer, and since $\nabla \cdot \vec{J} = 0$, one then has

$$\vec{V} \cdot \nabla \left[\frac{1}{2}V^2 + \frac{\gamma}{\gamma-1}\frac{P}{\rho} + \frac{B_\theta^2}{\mu_0\rho}\right] = \left(\frac{m_i}{e}\right)\frac{1}{\rho}\vec{J} \cdot \nabla \left[\frac{B_\theta^2}{\mu_0\rho}\right] \quad . \tag{A-19}$$

In terms of the generalized cylindrical coordinates, Eq. (A-19) can be expressed as

$$\frac{\partial}{\partial z}(h) = \vec{\epsilon}_H \cdot \nabla \left(\frac{B_\theta^2}{\mu_0\rho}\right) \tag{A-20}$$

47

where, now,

$$\vec{\epsilon}_H \equiv \frac{\vec{J}}{neV} \quad .$$

(A-21

and

$$h = \frac{1}{2}V^2 + \frac{\gamma}{\gamma - 1}\frac{P}{\rho} + \frac{B_\theta^2}{\mu_0\rho} = h_{\text{plas.}} + \frac{B_\theta^2}{\mu_0\rho}$$

is the generalized specific enthalpy.

The relative variation of h in moving a significant distance (δz) along a plasma (fluid-ion) streamline is thus

$$\frac{\delta h}{h} = \epsilon_{Hx}\frac{(B_\theta^2/\mu_0\rho)}{\left[(B_\theta^2/\mu_0\rho) + h_{\text{plas.}}\right]}\left\{\frac{(\delta z)}{(B_\theta^2/\mu_0\rho)}\frac{\partial}{\partial x}\left(\frac{B_\theta^2}{\mu_0\rho}\right)\right\}$$

$$+ \epsilon_{Hz}\frac{(B_\theta^2/\mu_0\rho)}{\left[(B_\theta^2/\mu_0\rho) + h_{\text{plas.}}\right]}\left\{\frac{(\delta z)}{(B_\theta^2/\mu_0\rho)}\frac{\partial}{\partial z}\left(\frac{B_\theta^2}{\mu_0\rho}\right)\right\} \quad .$$

(A-22

From (A-21) together with (A-7) and (A-9), it then can be inferred from (A-22) that either small Ξ, or a quasi-1D configuration with weak transverse gradients and small β_i suffices to produce only a small relative error in h over a significant distance δz.

APPENDIX B

SELF-CONSISTENT THERMAL EFFECTS

In the main text, in the interests of a simpler presentation, we outlined the quasi-1D formulation of the self-field, cold-flow model, and presented the results therefrom, as applied to 10MW-10ms-class experiments in the CTX device. The values of ion "beta" $(2\mu_0 P_i / B_\theta^2)$ were inferred *a posteriori*. In this Appendix, the self-field flow model is developed, now self-consistently including thermal effects. However, we shall again make the restriction to $\gamma = 2$ for the sake of simplicity. It follows that the value of beta is constant along the flow. (The electron contribution to the plasma pressure is neglected in view of the measurements of low electron temperatures compared with the inferred ion temperatures.)

Now, the full value of the generalized specific enthalpy as given by Eq. (5) is conserved along the flow. For $\gamma = 2$, h may be written as

$$h \equiv \frac{1}{2}V^2 + \frac{2P}{\rho} + \frac{B_\theta^2}{\mu_0 \rho} = \frac{1}{2}V^2 + \frac{B_\theta^2}{\mu_0 \rho}(1 + \beta) = \text{ const. } , \qquad \text{(B-1)}$$

and the flow velocity through the throat of an annular constriction, Eq. (11), may be written as

$$V_0^2 = C_{A0}^2 + C_{S0}^2 = C_{A0}^2(1 + \beta) , \qquad \text{(B-2)}$$

wherein C_A and C_S have been defined in Eq. (10).

By means of the quasi-1D form of mass-conservation, together with Eq. (6-a), one now finds

$$\frac{\Delta_b}{\Delta_0} \frac{V_b}{C_{Ab}} = \left(\frac{\rho_0}{\rho_b}\right)^{3/2} \sqrt{1 + \beta} , \qquad \text{(B-3)}$$

which replaces Eq. (16).

With $x_0 \equiv (\rho_0 / \rho_b)$, Eq. (B-3) also can be written as

$$x_0^3 = \left(\frac{\Delta b}{\Delta_0}\right)^2 \left(\frac{V_b}{C_{Ab}}\right)^2 \frac{1}{(1 + \beta)} \qquad \text{(B-3-a)}$$

Now, invoking the constancy of h (Eq. (B-1)) between breech and throat, together with Eq. (B-3), one can derive

$$\left[\frac{1}{2}\frac{V_b^2}{C_{Ab}^2}\frac{1}{1 + \beta} + 1\right]^{3/2} = \left(\frac{3}{2}\right)^{3/2}\left(\frac{\Delta_b}{\Delta_0}\frac{V_b}{C_{Ab}}\right)\frac{1}{\sqrt{1 + \beta}} = \left(\frac{3}{2}\frac{\rho_0}{\rho_b}\right)^{3/2} . \qquad \text{(B-4)}$$

Now, one finds that, in the limit that $V_b^2 \ll C_{Ab}^2$, the density ratio becomes

$$\frac{\rho_0}{\rho_b} \approx \frac{2}{3}, \quad \left(\text{for } \frac{V_b^2}{C_{Ab}^2} \ll 1\right) .$$

49

which is the same result as for cold flow.

At this point, we shall invoke the ion-entrainment-heating model. According to this model, β is not an independent parameter, but is related to the upstream Alfvén-Mach number according to the equipartition between flow energy and thermal energy. This is given by Eq. (29) and reads as

$$\beta = \frac{V_b^2}{C_{Ab}^2} \ . \tag{B-5}$$

Now, Eq. (B-4) becomes

$$\left[\frac{1}{2}\frac{\beta}{1+\beta} + 1\right]^{3/2} = \left(\frac{3}{2}\right)^{3/2} \frac{\Delta_b}{\Delta_0} \sqrt{\frac{\beta}{1+\beta}} \ . \tag{B-6}$$

From this equation, for a given β one can find (Δ_b/Δ_0), and then (ρ_0/ρ_b) from Eq. (B-4).

Equation (B-6) also can be written as

$$A\zeta^3 - \zeta^2 + \frac{1}{2} = 0 \ , \tag{B-7}$$

where

$$A \equiv \left(\frac{2}{3}\right)^{3/2} \frac{\Delta_0}{\Delta_b} \ , \tag{B-8}$$

and

$$\zeta \equiv \sqrt{\frac{1+\beta}{\beta} + \frac{1}{2}} \ . \tag{B-9}$$

The formulation in Eq. (B-7) is useful when one has prior information regarding the contraction ratio (Δ_b/Δ_0), in which case one can solve the cubic equation (B-7) for β and thus for the upstream Alfvén-Mach number. In the present set of experiments, that information is lacking; so, instead we shall solve Eq. (B-6) for (Δ_b/Δ_0) and then (B-4) for (ρ_0/ρ_b), both as functions of β. The results are plotted (vs. $\sqrt{\beta}$) as the dotted curves in Fig. (14). We see that for small-to-moderate values of $\sqrt{\beta} \equiv V_b/C_{Ab}$, say for $\sqrt{\beta} \lesssim 0.7$, there are only minor differences from the cold-flow results.

Next, we relate the discharge resistance to the upstream Alfvén-Mach number, including thermal effects. Beginning with the discharge voltage expressed across the throat of a presumed nozzle,

$$\mathbf{V} = E_r \Delta_0 = V_0 B_{\theta 0} \Delta_0 \ ,$$

and recalling that $V_0 = C_{A0}\sqrt{1+\beta}$, one finds

$$\mathbf{V} = \Delta_0 x_0^2 \left(\frac{\mu_0 I}{2\pi r}\right)^2 \frac{\sqrt{1+\beta}}{\sqrt{\mu_0 \rho_0}} \ . \tag{B-10}$$

50

Here, the conservation of (B_θ/ρ) between breech and throat was invoked.

But, with $\dot{M} = \rho_0 V_0 2\pi r \Delta_0$, and using the same conservation law, one can write

$$\frac{1}{\sqrt{\mu_0 \rho_o}} = \frac{x_0 I \Delta_0}{\dot{M}} \sqrt{1+\beta} \ . \tag{B-11}$$

The use of (B-11) in (B-10) yields the discharge resistance:

$$\mathbf{R} \equiv \frac{\mathbf{V}}{I} = \left(\frac{\Delta_0}{r}\right)^2 x_0^3 \left(\frac{\mu_0}{2\pi}\right)^2 \frac{I^2}{\dot{M}}(1+\beta) \ . \tag{B-12}$$

Substitution for x_0^3 from Eq. (B-3-a) then yields

$$\mathbf{R} = \left(\frac{\Delta_0}{r}\right)^2 \left[\left(\frac{\Delta_b}{\Delta_0}\right)^2 \frac{(V_b/C_{Ab})^2}{(1+\beta)}\right] \left(\frac{\mu_0}{2\pi}\right)^2 \frac{I^2}{\dot{M}}(1+\beta) \ . \tag{B-13}$$

We see therefore, that the extra factor $(1+\beta)$ exactly cancels out of this expression for the discharge resistance! Thus, Eqs. (27) and (28), which provide the expression for the upstream Alfvén-Mach number in terms of the global experimental parameters of the CTX device, I, $\mathbf{R}$, and $\dot{M}$, prove to be exact in ideal MHD with respect to thermal effects (assuming $\gamma = 2$)!

It follows that the three internal parameters that depend directly on the inferred value of (V_b/C_{Ab}) also must be exact within ideal MHD with respect to thermal effects. These parameters are the inferred β; $(r_{ci})_b$, the inferred ion gyro-radius upstream; and n_b, the inferred ion (or electron) number density upstream.

There are two other parameters, namely the nozzle contraction ratio (Δ_b/Δ_0), and the nozzle density ratio, (ρ_0/ρ_b), whose functional β-dependences do, in fact, depend thermally upon the inferred values of β. The thermal corrections to these parameters may be read from Fig. (14). For helium and deuterium, the upstream Alfvén-Mach numbers were inferred to be about 0.5, for which Fig. (14) indicates about a 7% increase should be applied to (Δ_b/Δ_0) and about a 1% decrease to (ρ_0/ρ_b). For argon, we found $V_b/C_{Ab} = 0.76$, indicating that (Δ_b/Δ_0) should be increased by about 12% whereas (ρ_0/ρ_b) should be decreased by about 8%. We conclude that thermal corrections appear to be not at all important in any of the gases studied here, within the context of ideal MHD. A more important source of error is probably the neglect of the Hall effect, especially in the case of argon. (See Appendix A.)

APPENDIX C

THE FIELD LINE STRETCHING MODEL

A simple one-dimensional model possessing axial and azimuthal symmetry can capture the distortion of the applied transverse magnetic flux engendered by the given flow of a resistive fluid in a perfectly conducting channel. For further simplification, we also assume slab geometry appropriate to a thin-channel model ($\Delta \ll r$). In CTX, $\Delta \approx 0.43r$. Sample calculations in full cylindrical coaxial geometry with $\Delta = 0.43r$ have been performed, but are much more complicated to describe. The results prove to differ very little from those obtained in slab geometry.

The purpose of this calculation is to estimate the stretching distance experienced by a transverse (poloidal) field line, and then to compare that distance with the observed displacement of the applied flux as measured by means of magnetic probes. A vacuum-field calculation of the applied flux provides the initial positions of the flux surfaces, and agrees well with special measurements of the vacuum field as described in the main text. The good agreement of this simple model with the observed flux displacement thus provides an heuristic means of understanding the extent of the displacement of the applied flux in CTX. The Hall effect proves to be an essential ingredient in this model "explanation" of the displacement.

In this 1-D model, the radial current must vanish, $J_x = 0$, else the azimuthal magnetic field B_y would acquire a dependence upon the axial spatial variable z, and the problem then would become a complicated two-dimensional calculation. Here, x and y respectively signify the radial and azimuthal coordinate variables in a slab geometry. A way to rationalize this point of view with no radial current is to imagine that the plasma has been pre-accelerated before it encounters the applied magnetic field so that the driving self-field, $B_y(z)$, already has been depleted upstream.

Another consequence of the 1-D model assumption, following from $\nabla \cdot \vec{B} = 0$, is that the radial field component, B_x, is independent of radial position, x.

Moreover, in a steady-state situation with axisymmetry, it follows from Faraday's law that the electric-field component $E_\theta = 0$, where θ is the azimuthal angle variable in cylindrical geometry. The slab-geometry analog of this condition is that the azimuthal electric field $E_y = 0$.

Finally, the steady-state condition $\nabla \times \vec{E} = 0$, contains the azimuthal component that reads.

$$-\frac{\partial}{\partial x}E_z + \frac{\partial}{\partial z}E_x = 0 \ .$$

In view of the assumed independence of E_x with respect to the axial coordinate z, the above reduces to the statement that E_z is independent of the radial coordinate

x. But, since the channel walls are taken to be electrically perfectly conducting, E_z must vanish at the walls; hence E_z must vanish everywhere within the channel, $E_z = 0$.

On the basis of the above-described model, we now can examine the components of Ohm's law including the Hall term,

$$\vec{E} + \vec{V} \times \vec{B} = \eta \vec{J} + \frac{1}{ne} \vec{J} \times \vec{B} \qquad \text{(C-1}$$

Here, $\vec{V}$ is the plasma velocity, $\vec{J}$ is the current density, $\eta = \frac{m_e \nu_e}{ne^2}$ is the resistivity of plasma, and n is the number-density of electrons with individual electrical charge e.

It is convenient to rewrite this in the form

$$\vec{E} + \vec{V} \times \vec{B} = D \left(\mu_0 \vec{J} + \Omega_x \frac{\mu_0 \vec{J} \times \vec{B}}{B_x} \right) \quad . \qquad \text{(C-2}$$

In (C-2), $D = (\eta/\mu_0)$ is the resistive diffusivity of plasma, and $\Omega_x = (eB_x/m_e\nu_e)$ is the electron-Hall parameter in the radial-magnetic-field component B_x. Also, m_e is the mass of an electron, and ν_e represents the momentum-transfer collision frequency of an average electron with the plasma ions.

Given the conditions of our 1-D model, we have seen that $J_x = 0$, $E_y = 0$, and $E_z = 0$. Therefore the y and z components of the Eq. (C-2) become, in the absence of radial velocity V_x,

$$\frac{V_z B_x}{D} = (\mu_0 J_y) + \Omega_x(\mu_0 J_z) \qquad \text{(C-3-a}$$

$$-\frac{V_y B_x}{D} = (\mu_0 J_z) - \Omega_x(\mu_0 J_y) \qquad \text{(C-3-b}$$

Here, a rotational velocity V_y is allowed for generality.

Solving for the currents, we find

$$\mu_0 J_y = \frac{1}{1 + \Omega_x^2} \{V_z + \Omega_x V_y\} \frac{B_x}{D} \qquad \text{(C-4-a}$$

$$\mu_0 J_z = \frac{1}{1 + \Omega_x^2} \{\Omega_x V_z - V_y\} \frac{B_x}{D} \qquad \text{(C-4-b}$$

Consider Eq. (C-4-a). In view of Ampere's law, $\nabla \times \vec{B} = \mu_0 \vec{J}$, this equation can be written as

$$\frac{\partial}{\partial \xi} \left(\frac{B_z}{B_x} \right) = -R_m H_\Omega \quad , \qquad \text{(C-5}$$

where ξ is a normalized radial coordinate given by

$$\xi \equiv x/\Delta \ , \qquad -\frac{1}{2} \leq \xi \leq \frac{1}{2} \ , \qquad \text{(C-6}$$

with Δ being the channel width, and in which we have chosen $x = 0$ in midchannel. Also, R_m is the magnetic Reynolds number defined as

$$R_m \equiv \frac{V_z \Delta}{D} \quad . \tag{C-7}$$

Finally, H_Ω is a function of the electron-Hall parameter that is given by

$$H_\Omega \equiv \frac{1 + \Omega_x \frac{V_y}{V_z}}{1 + \Omega_x^2} \quad . \tag{C-8}$$

Integrating (C-5) gives

$$\frac{B_z}{B_x} = -R_m H_\Omega \xi + \left(\frac{B_z}{B_x}\right)_0 \tag{C-9}$$

where subscript "0" signifies evaluation at midchannel, at $\xi = 0$.

The differential equation of the $(x,\ z)$ projection of a distorted field line is given by

$$\frac{B_z}{B_x} = \frac{d\zeta}{d\xi} \quad , \tag{C-10}$$

where we have defined a normalized axial coordinate as

$$\zeta \equiv z/\Delta \quad . \tag{C-11}$$

We shall choose $\zeta = 0$ at the cathode foot-point of the magnetic field line, where $\xi = -1/2$.

Using (C-10) in (C-9) and integrating again, one has

$$\zeta(\xi) = -R_m H_\Omega \frac{\xi^2}{2} + \left(\frac{B_z}{B_x}\right)_0 \xi + \zeta_0 \tag{C-12}$$

This is the equation of the $(x,\ z)$ projection of a distorted magnetic field line. The condition that $\zeta = 0$ at $\xi = -1/2$ determines ζ_0. With that determination, (C-12) becomes

$$\zeta(\xi) = -R_m H_\Omega \left(\frac{\xi^2}{2} - \frac{1}{8}\right) + \left(\frac{B_z}{B_x}\right)_0 \left(\xi + \frac{1}{2}\right) \quad . \tag{C-13}$$

Here we note that, in principle, the field-line slope at midchannel, $(B_z/B_x)_0$, can depend on the plasma parameters R_m and H_Ω.

The "vacuum" equation for a field line is obtained either from the condition of infinite resistivity or from zero flow ($V_z = 0,\ V_y = 0$). In either case, one has $(R_m H_\Omega) = 0$, and (C-13) reduces to

$$\zeta_{\text{vac}}(\xi) = (B_z/B_x)_{\text{vac},\ 0}\ (\xi + 1/2) \quad . \tag{C-14}$$

Thus, within the slab-geometry model, the vacuum field lines are straight lines, with $(B_z/B_x)_{\text{vac}}$ being independent of ξ.

54

Therefore the axial distance between the cathode and anode footpoints of a vacuum field line is given by

$$\zeta_{\text{vac}}(1/2) = (B_z/B_x)_{\text{vac}} \quad . \tag{C-15}$$

Since the walls are perfect electrical conductors, the distance between cathode and anode footpoints remains fixed as the plasma flow is imagined to be increased from zero, or as the plasma electrical conductivity is increased from zero. Therefore, that distance as represented by $\zeta(1/2)$ in the case of flowing plasma, should be the same distance as $\zeta_{\text{vac}}(1/2)$. But from Eq. (C-13), one has this footpoint separation as

$$\zeta(1/2) = (B_z/B_x)_0 \quad . \tag{C-16}$$

Thus, the "frozen-in footpoint" condition is realized by equating (C-15) and (C-16), which yields

$$(B_z/B_x)_0 = (B_z/B_x)_{\text{vac}} \quad . \tag{C-17}$$

Thus, the slope of the distorted field line, at midchannel, must be the same as the slope of the straight, vacuum field line.

Therefore, Eq. (C-13) can be written as

$$\zeta(\xi) = \frac{1}{8} R_m H_\Omega \left(1 - 4\xi^2\right) + (B_z/B_x)_{\text{vac}} \left(\xi + \frac{1}{2}\right) \quad . \tag{C-18}$$

The vacuum field line is a straight line (in the slab approximation) which becomes distorted into a parabola by the fixed plasma flow. The axially stretched field line would have exerted a back-reaction causing the plasma to slow down in a self-consistent model.

In a similar treatment, Eq. (C-4-b) for J_z can be shown to involve the simultaneous stretching of the vacuum field line into the azimuthal direction. The Hall effect will bring about this azimuthal stretching even when there is no *a-priori* rotation of plasma. (Of course the back-reaction of this azimuthally stretched field line would cause the plasma to rotate in a self-consistent model.)

Returning to (C-18), let us define the "stretching constant," K_z, for the z-direction as

$$K_z = R_m H_\Omega \tag{C-19}$$

and write

$$\zeta(\xi) = \frac{1}{8} K_z (1 - 4\xi^2) - |B_z/B_x|_{\text{vac}}(\xi + 1/2) \tag{C-20}$$

In the cases considered here, $B_x > 0$ and $B_{z,\text{vac}} < 0$. The stretching constant, K_z, constitutes an "effective magnetic Reynolds number," which reduces to the usual R_m in the limit of no Hall effect. Eq. (C-20) is the equation of the shape of the field line as given in the main text.

55

We shall measure the stretching distance (in terms of Δ) from the cathode footpoint to the "nose" of the field line, defined as the value of $\zeta(\xi)$ at which $\zeta'(\xi) = 0$. A simple calculation then shows that the nose of the parabola occurs at

$$\xi_{\text{nose}} = -\frac{1}{K_z}|B_z/B_x|_{\text{vac}} \qquad \text{(C-21-a}$$

and

$$\zeta_{\text{nose}} = \frac{1}{2}K_z \left(\frac{1}{2} - \frac{1}{K_z}|B_z/B_x|_{\text{vac}}\right)^2 \ . \qquad \text{(C-21-b}$$

Thus, a purely radial field line would become distorted into a symmetrical parabola in which $\zeta'(\xi) = 0$ at midchannel, $\xi = 0$, and the stretching distance would become $\frac{1}{8}K_z$. This remains almost true for moderately oblique field lines, as long as the stretching constant, K_z, is large compared with $|B_z/B_x|_{\text{vac}}$. Note that this stretching distance is severely limited by the presence of a large electron-Hall parameter, $\Omega_x^2 \gg 1$; see (C-8) and (C-19). This effect is due to the enlarged electron "magneto-resistance;" see Eq. (C-4-a). Thus, the large effective resistivity engendered by the Hall effect allows the axially flowing plasma to exert a smaller resistive drag on the transverse field lines, smaller in comparison to the drag that would have been exerted in a model without the Hall effect.

TABLE II:

Data and inferences for helium discharges. Self-consistent thermal effects are included.

gas = helium;   ion mass number = 4; $V_{CIV} = 3426$ [sec.] $\equiv 0.1\, V_{CIV}$ [m/s] for He⁺

$$R_{[m\Omega]}^{(CIV)} = 10^{-3}\, V_{CIV}\ \text{[sec.]} \approx 3.4\ m\Omega$$

	experimental data							inferred results							
i.d.#	pfc_{amps}	I_{KA}	V_{volts}	$R_{m\Omega}$	$\dot{M}_{g/s}$	Ξ	n_e (meas.) [cm⁻³]	$\sqrt{\beta}$	β	(Δ_b/Δ_o)	(ρ_o/ρ_b)	$\dfrac{2r_{cit}}{\Delta_b}$	$(\sqrt{\beta})_{CIV}$	n_{eb}(CIV) [cm⁻³]	remarks ($t_{av.}$ - ms)
266	144	60.0	150	2.5	4.0	0.63	0.60 x 10¹⁴	0.61	0.37	1.27	0.76	0.46	0.66	1.0 x 10¹⁴	2-10, a
247	141	29.6	70.7	2.4	2.25	0.55	0.31	0.90	0.81	1.10	0.82	0.89	1.0	0.54	5-10, b
297	141	60.0	182	3.0	2.25	1.12	0.75	0.50	0.25	1.40	0.73	0.56	0.50	0.69	5-10, a
305	140	60.0	180	3.0	2.25	1.12	0.50	0.50	0.25	1.41	0.73	0.55	0.50	0.68	5-10, c
628	140	38.0	91.9	2.4	2.25	0.71	1.1	0.71	0.50	1.19	0.78	0.71	0.78	0.55	3-7, d
395	140	40.3	112	2.8	2.25	0.75	0.28	0.71	0.51	1.18	0.78	0.77	0.74	0.63	3-10, d

remarks: (Location of n_e (meas.) relative to muzzle and to cathode.)

a) 1 cm downstr.; 5 cm from cathode.

b) 5 cm downstr; 5 cm from cathode.

c) 5 cm upstream; 2.5 cm from cathode.

d) 5 cm upstream; 5 cm from cathode.

TABLE III:

Data and inferences for argon discharges. Self-consistent thermal effects are included.

gas = argon;   ion mass number = 40; $V_{CIV} = 1439$ [sec.] $\equiv$ 0.1 V_{CIV} [m/s] for Ar^{++}

$R_{[m\Omega]}^{(CIV)} = 10^{-3} V_{CIV}$ [sec.] $\approx$ 1.4 mΩ

| | | | | | | | experimental data | | | inferred results | | | | | |
i.d.#	pfc$_{amps}$	IKA	V$_{volts}$	R$_{m\Omega}$	$\dot{M}$ g/s	Ξ	n_e (meas.) [cm^{-3}]	$\sqrt{\beta}$	β	(Δ_b/Δ_o)	(ρ_o/ρ_b)	$\dfrac{2r_{cib}}{\Delta_b}$	$(\sqrt{\beta})_{CIV}$	n_{eb}(CIV) [cm^{-3}]	remarks (tav. - ms)
493	220	64.6	92.7	1.4	10.0	2.71	2.6 × 10^{14}	0.67	0.45	1.21	0.77	1.23	0.63	1.6 × 10^{14}	5-10, d
494	140	63.4	111	1.7	10.0	2.66	2.6	0.76	0.57	1.16	0.79	1.53	0.64	2.0	7-13, d
496	182	66.0	98.3	1.5	10.0	2.77	2.8	0.67	0.45	1.21	0.77	1.25	0.62	1.7	5-10, d
660	280	65.8	80.3	1.2	10.0	2.76	0.81	0.61	0.37	1.26	0.76	1.03	0.62	1.4	5-10, e

remarks: (Location of n_e (meas.) relative to muzzle and to cathode.)

a)

b)

c)

d) 5 cm upstream; 5 cm from cathode.

e) 5 cm upstream; 7.5 cm from cathode

58

TABLE IV:

Data and inferences for deuterium discharges. Self-consistent thermal effects are included.

gas = deuterium;   ion mass number = 2; $V_{CIV} = 5500$ [sec.] $\equiv 0.1\ V_{CIV}$ [m/s] for $D_2 \rightarrow D^+ + D^+$

$R_{[m\Omega]}^{(CIV)} = 10^{-3}\ V_{CIV}$ [sec.] $= 5.5\ m\Omega$

i.d.#	pfc $_{amps}$	I$_{kA}$	V$_{volts}$	R$_{m\Omega}$	$\dot{M}_{g/s}$	Ξ	n_e(meas.) [cm^{-3}]	$\sqrt{\beta}$	β	(Δ_b/Δ_o)	(ρ_o/ρ_b)	$\dfrac{2r_{cib}}{\Delta_b}$	$(\sqrt{\beta})_{CIV}$	n_{eb}(CIV) [cm^{-3}]	remarks ($t_{av.}$ - ms)
						experimental data						inferred results			
580	180	49.3	286	5.8	1.26	0.82	0.64 × 10^{14}	0.63	0.40	1.25	0.76	0.65	0.57	0.57 × 10^{14}	5-10, f
581	275	53.5	258	4.8	1.26	0.89	0.60	0.53	0.28	1.36	0.74	0.50	0.53	0.48	5-10, f
594	274	53.8	251	4.7	1.26	0.89	0.68	0.52	0.27	1.37	0.74	0.48	0.53	0.46	5-10, f
595	180	50.2	284	5.7	1.26	0.84	0.54	0.61	0.37	1.26	0.76	0.62	0.56	0.56	5-10, f
604	180	55.0	262	4.8	1.26	0.91	0.78	0.51	0.26	1.38	0.74	0.48	0.51	0.47	3-10, b
609	218	52.6	284	5.4	4.4	0.25	0.30	1.06	1.14	1.06	0.84	0.57	1.00	1.9	5-10, f
610	277	52.3	239	4.6	4.4	0.25	0.73	0.99	0.97	1.08	0.83	0.48	1.01	1.6	5-10, f

remarks: (Location of n_e (meas.) relative to muzzle and to cathode.)

a)

b) 5 cm downstream; 5 cm from cathode

c)

d)

e)

f) 0.5 cm downstream; 5 cm from cathode.
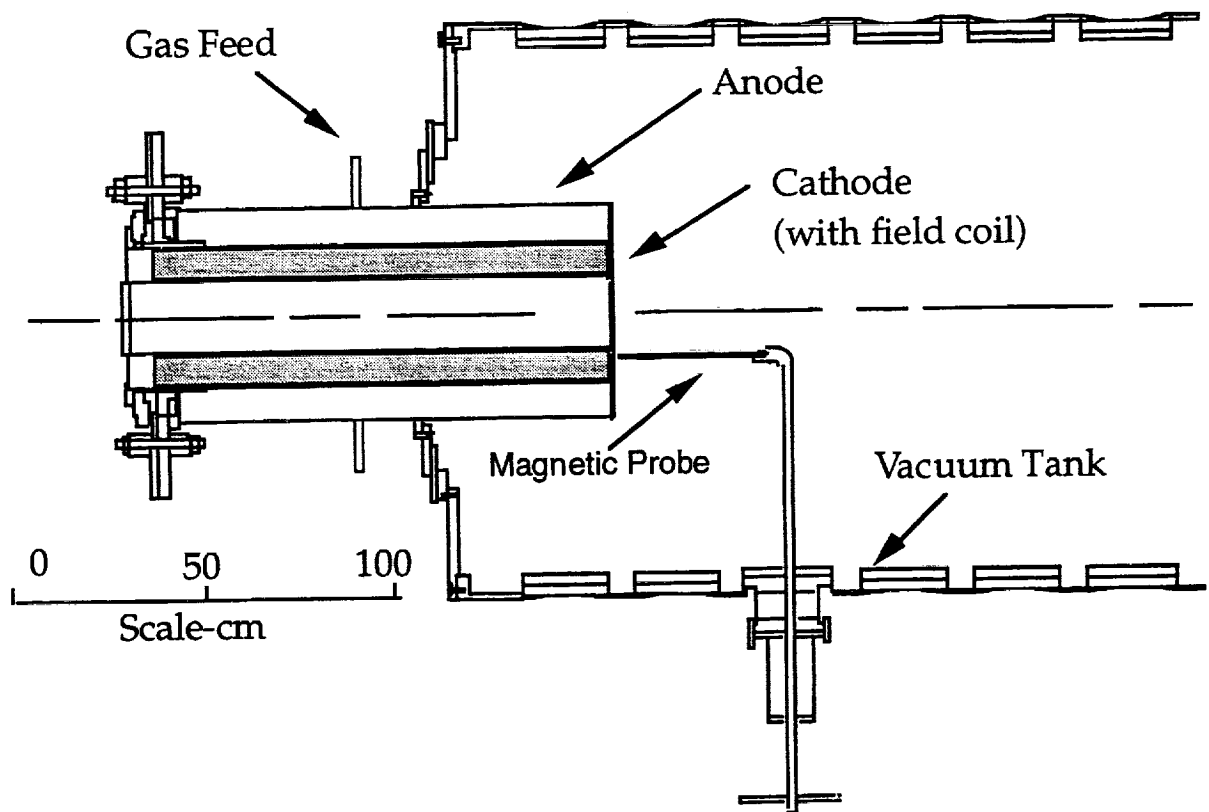
Figure 1. Schematic of CTX coaxial plasma thruster. The sliding and rotating vacuum feedthrough allows the magnetic probe to be positioned at different locations relative to the thruster.
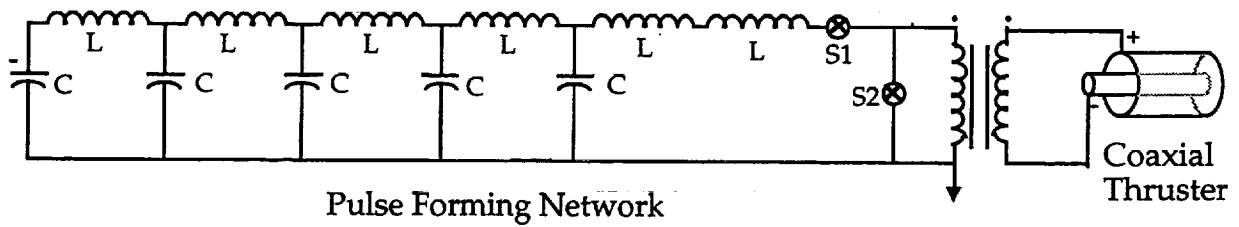
Figure 2. Schematic of CTX pulse forming network. C= 8 mF, and L = 0.125 mH. The transformer steps the voltage down by a ratio of 5 to 1.
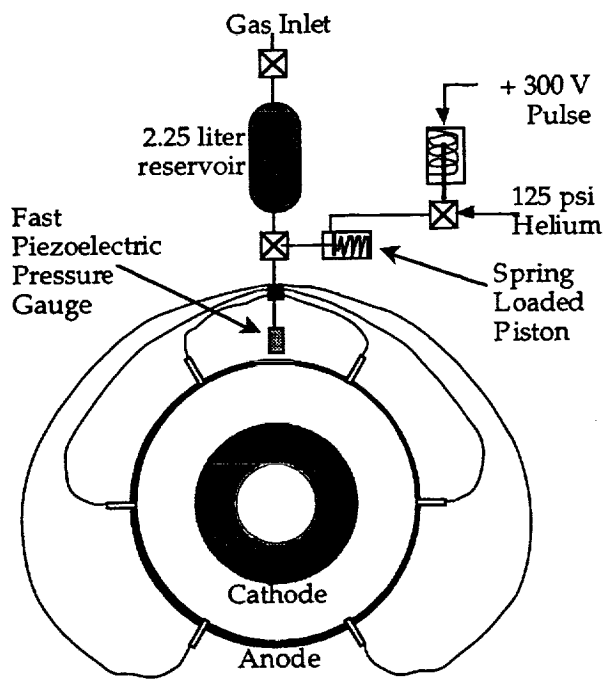
Figure 3. Schematic of long pulse gas valve system. The six stainless steel gas lines connecting the valve to the anode are of equal length.
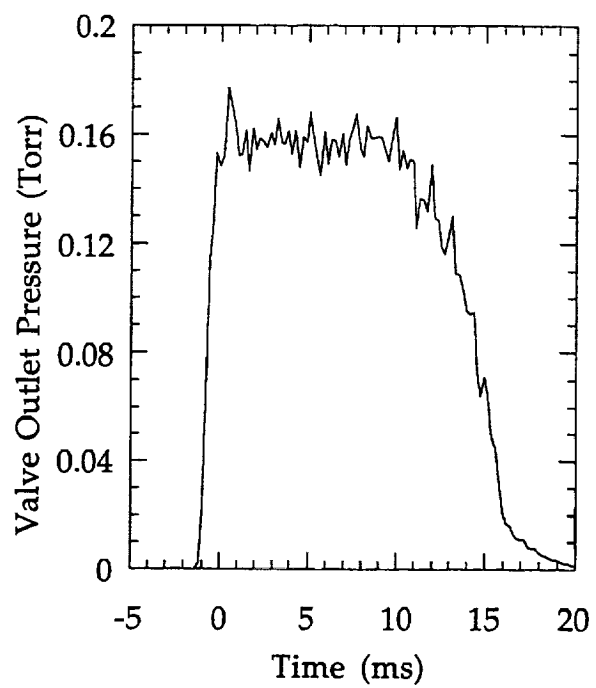
Figure 4. Long pulse gas valve outlet pressure as a function of time. Reservoir fill pressure was 5023 Torr helium. The valve was triggered at -5 ms.
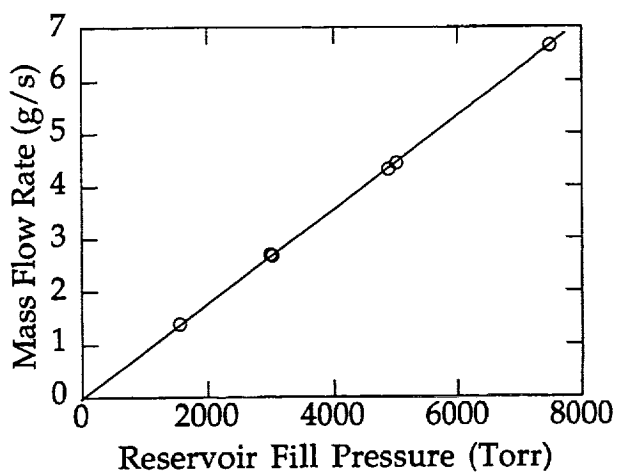
Figure 5. Mass flow rate of helium through long-pulse gas valve as a
function of reservoir fill pressure.
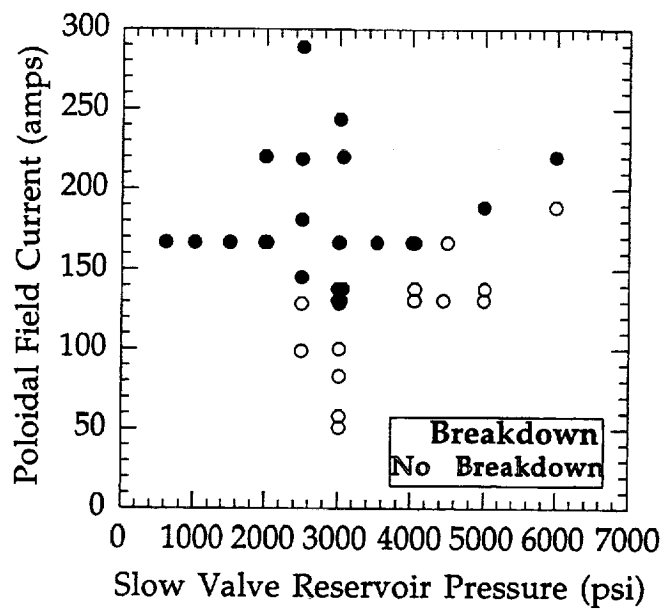
Figure 6. Operating regime for helium discharges showing combination of applied magnetic field coil current and propellant mass flow rate that produce thruster breakdown for a bank charge voltage of 2.5 kV.
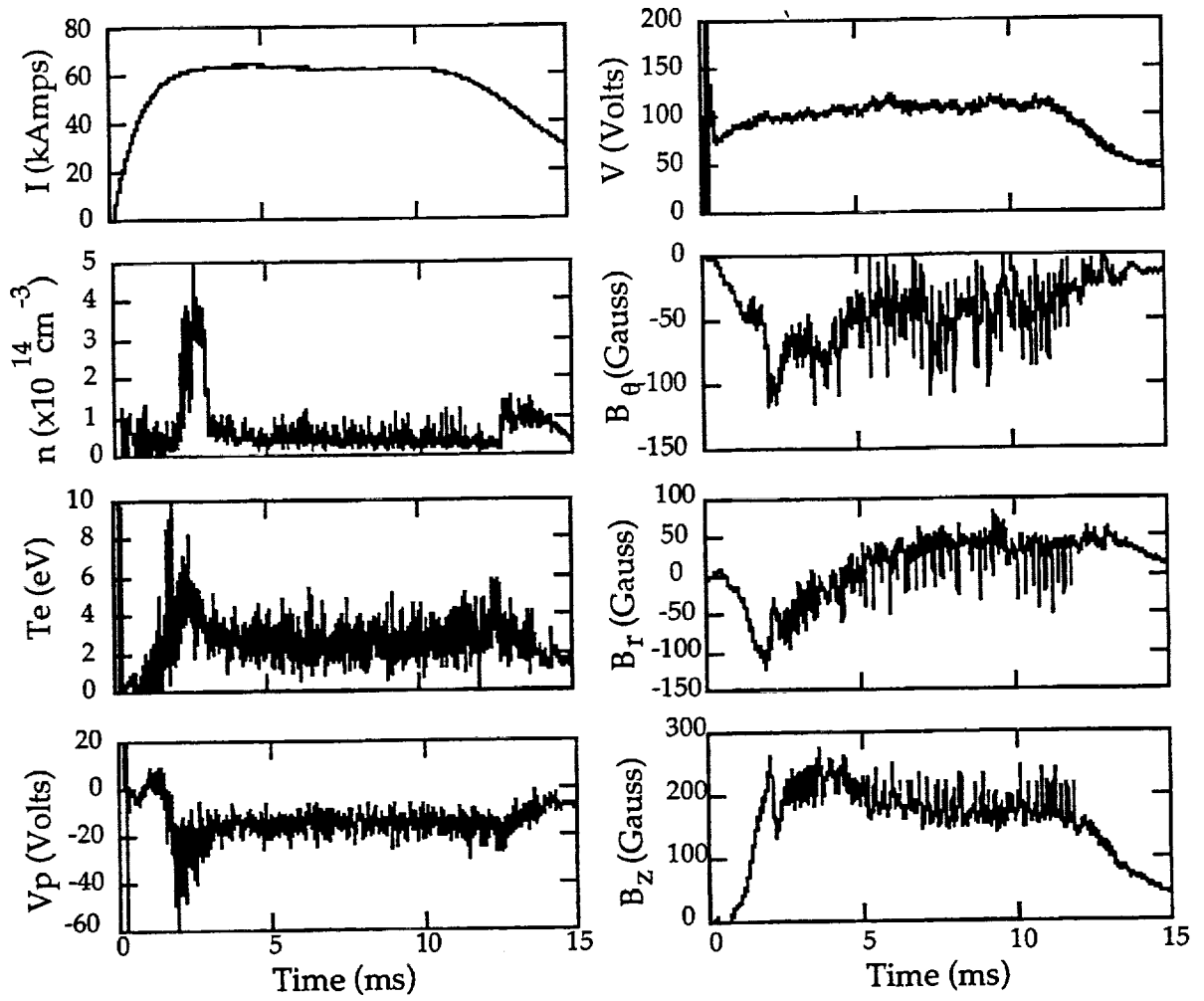
Figure 7. CTX thruster data for a 6 MW helium discharge with a gas feed rate of 6 g/s. Shown are the current I(kA), voltage V(volts), plasma density n (cm^{-3}), electron temperature Te(eV), plasma potential Vp(Volts), and magnetic field fluctuation components (Gauss) in the azimuthal (B$_q$), radial (B$_r$) and axial (B$_z$) directions.
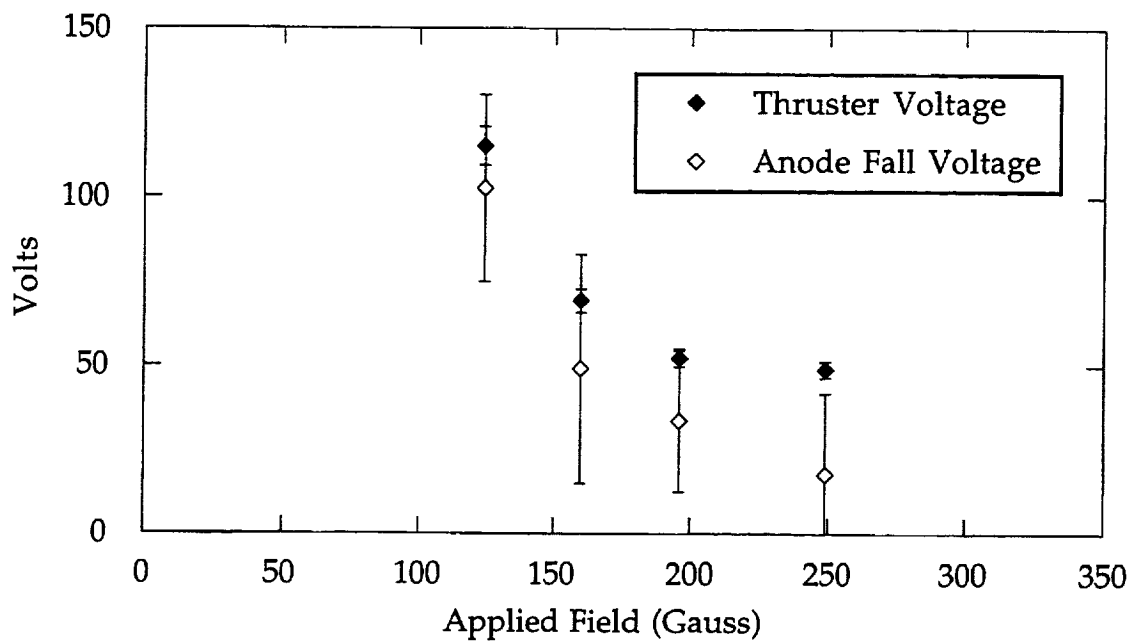
Figure 8. Total thruster voltage and anode fall voltage as a function of applied magnetic field strength for a 2.5 g/s helium discharge with a 3.5 kV bank charge voltage. Thruster power was approximately 2 MW.
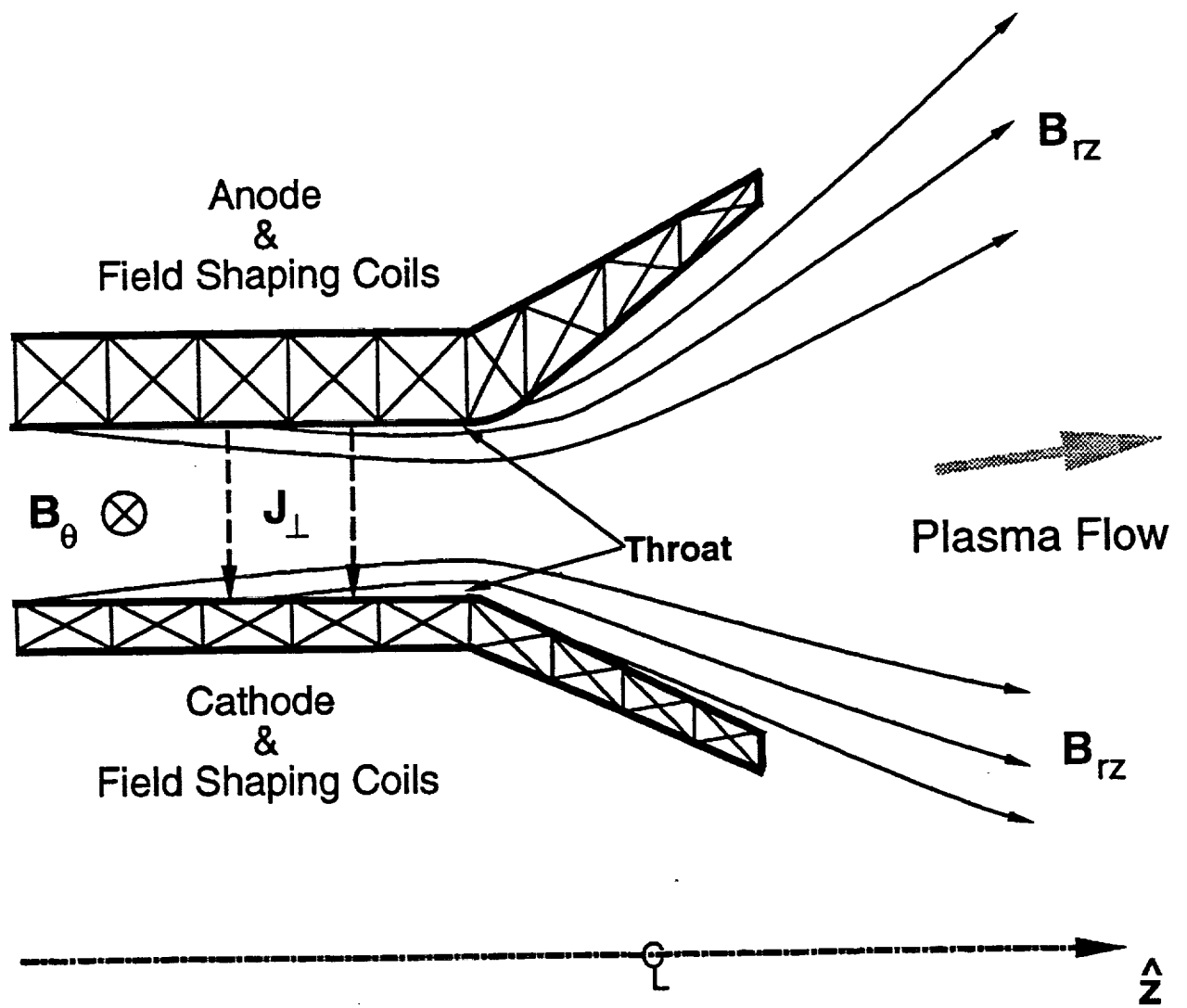
Figure. 9. Schematic of proposed thruster with applied nozzle field.
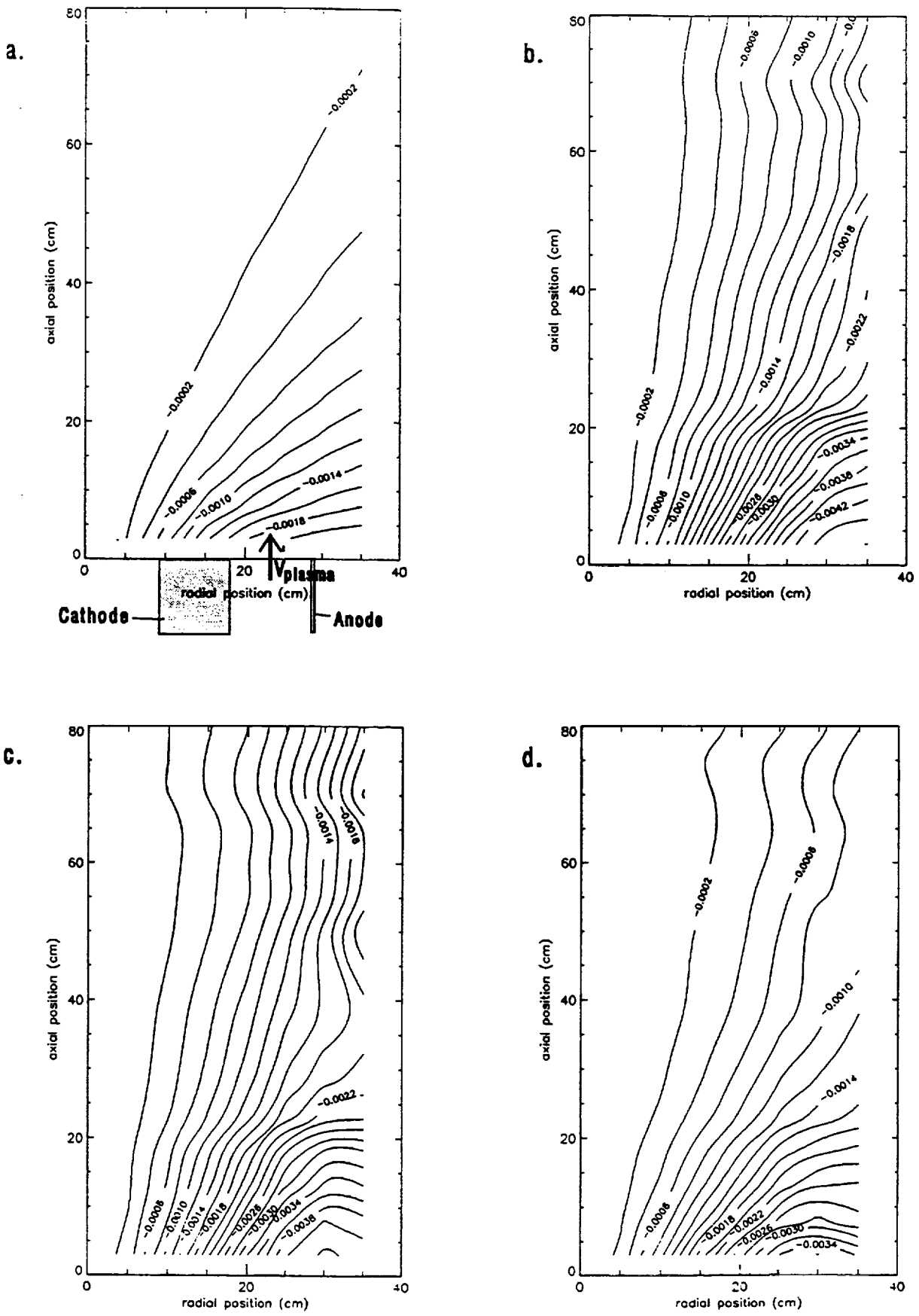
Figure 10. Contours of constant magnetic flux for a 6 MW helium discharge at (a) 0 ms, (b) 4 ms, (c) 10 ms, and (d) 14 ms.
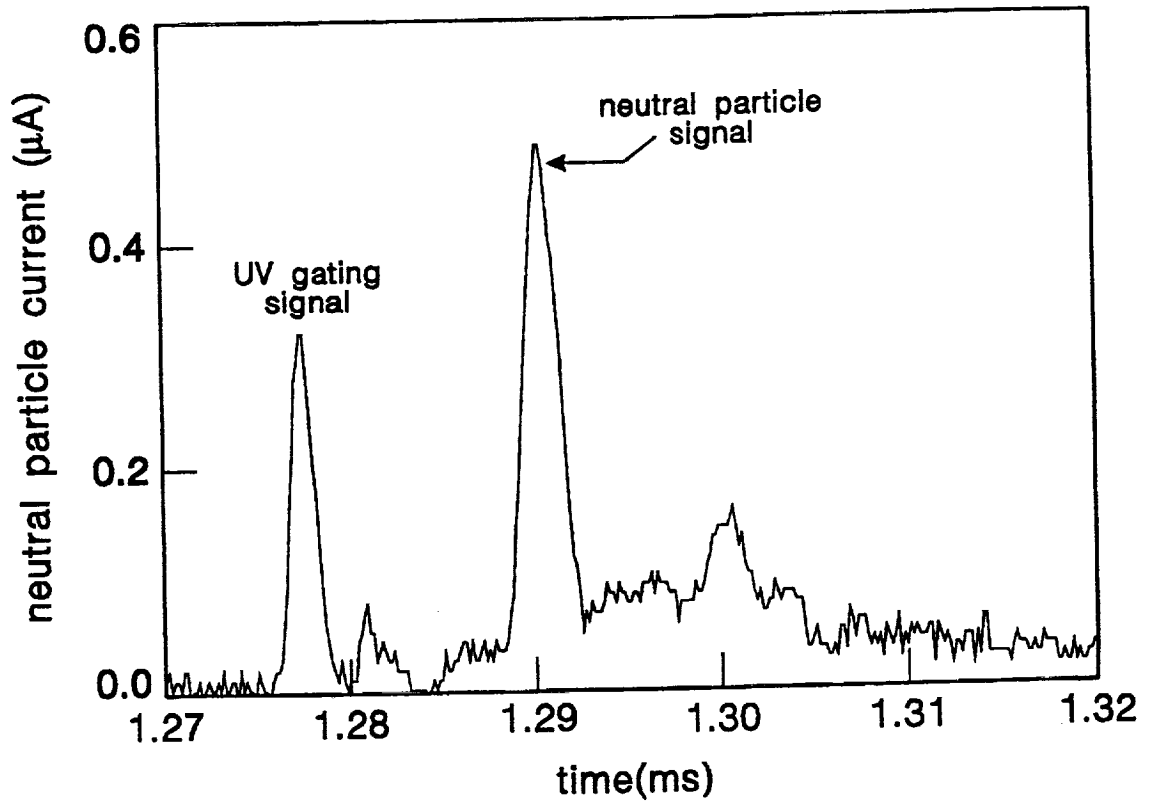
Figure 11. Neutral particle time-of-flight spectrometer signal.
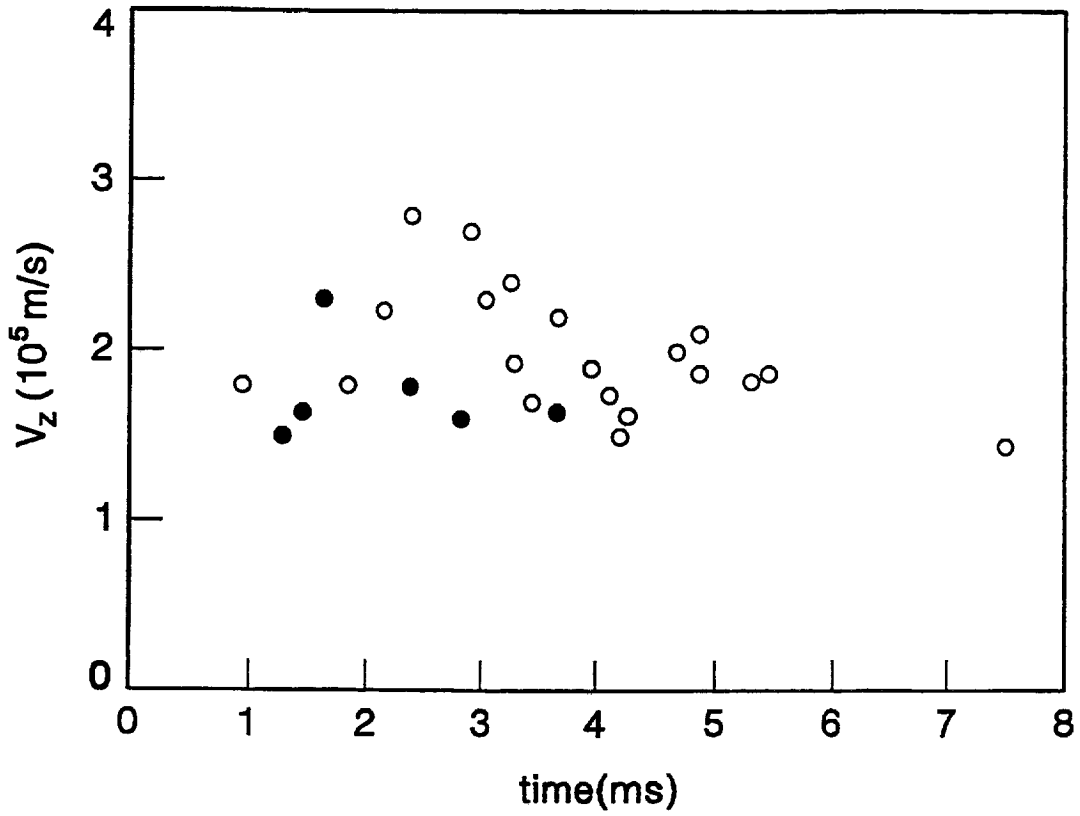
Figure 12. Reduced TOF data for 10 MW deuterium and helium CTX discharges.
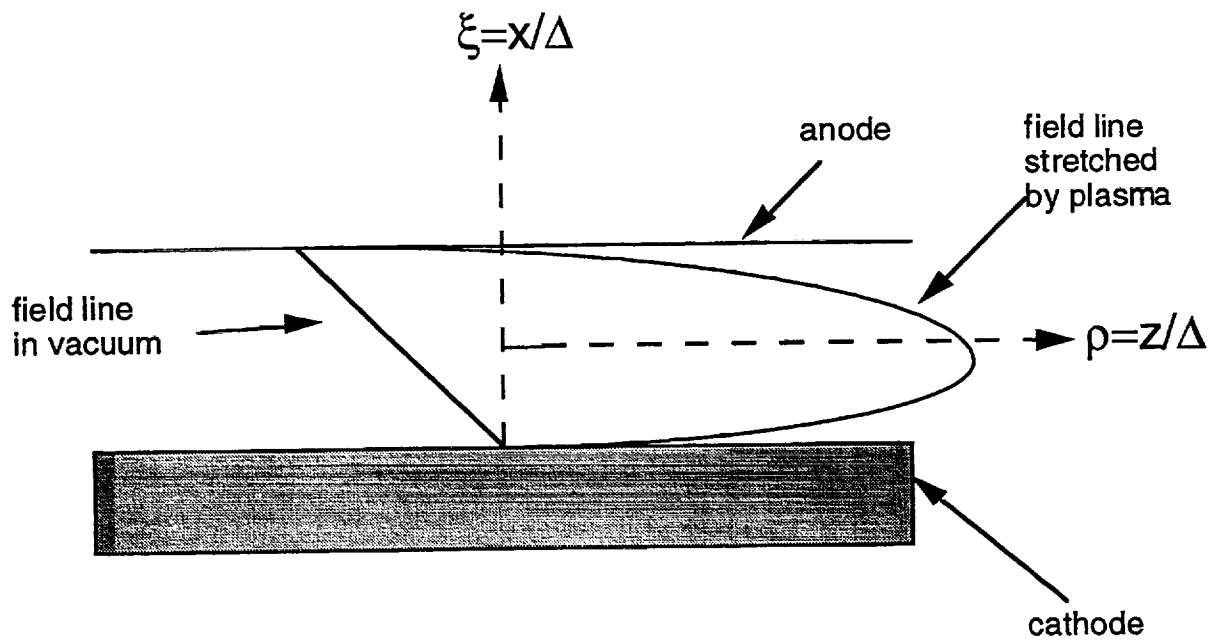
Figure 13. Schematic of model describing stretching of magnetic field lines.
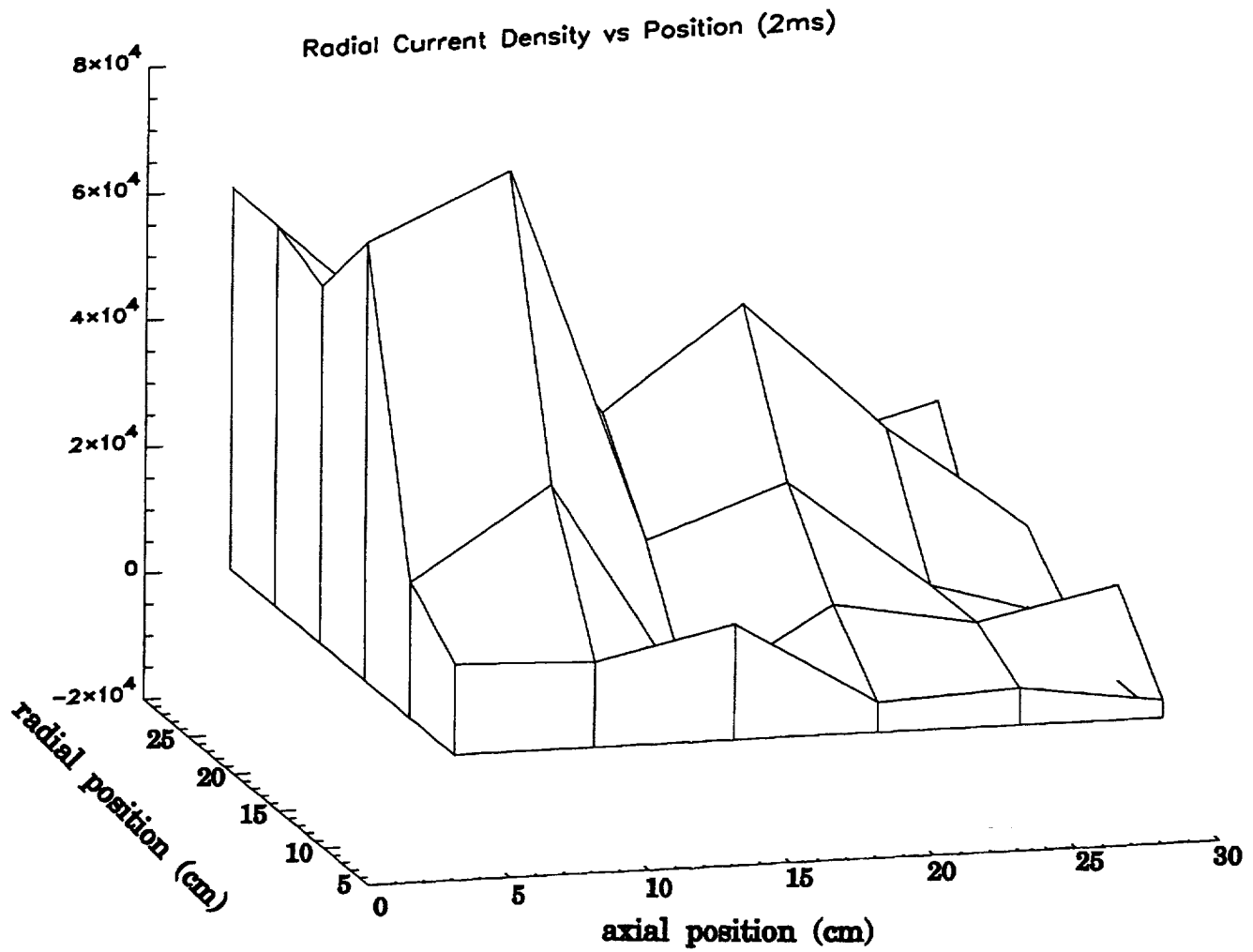
Figure 14 (a). Radial current density as a function of axial and radial position for a 6 MW discharge at t = 2 ms.
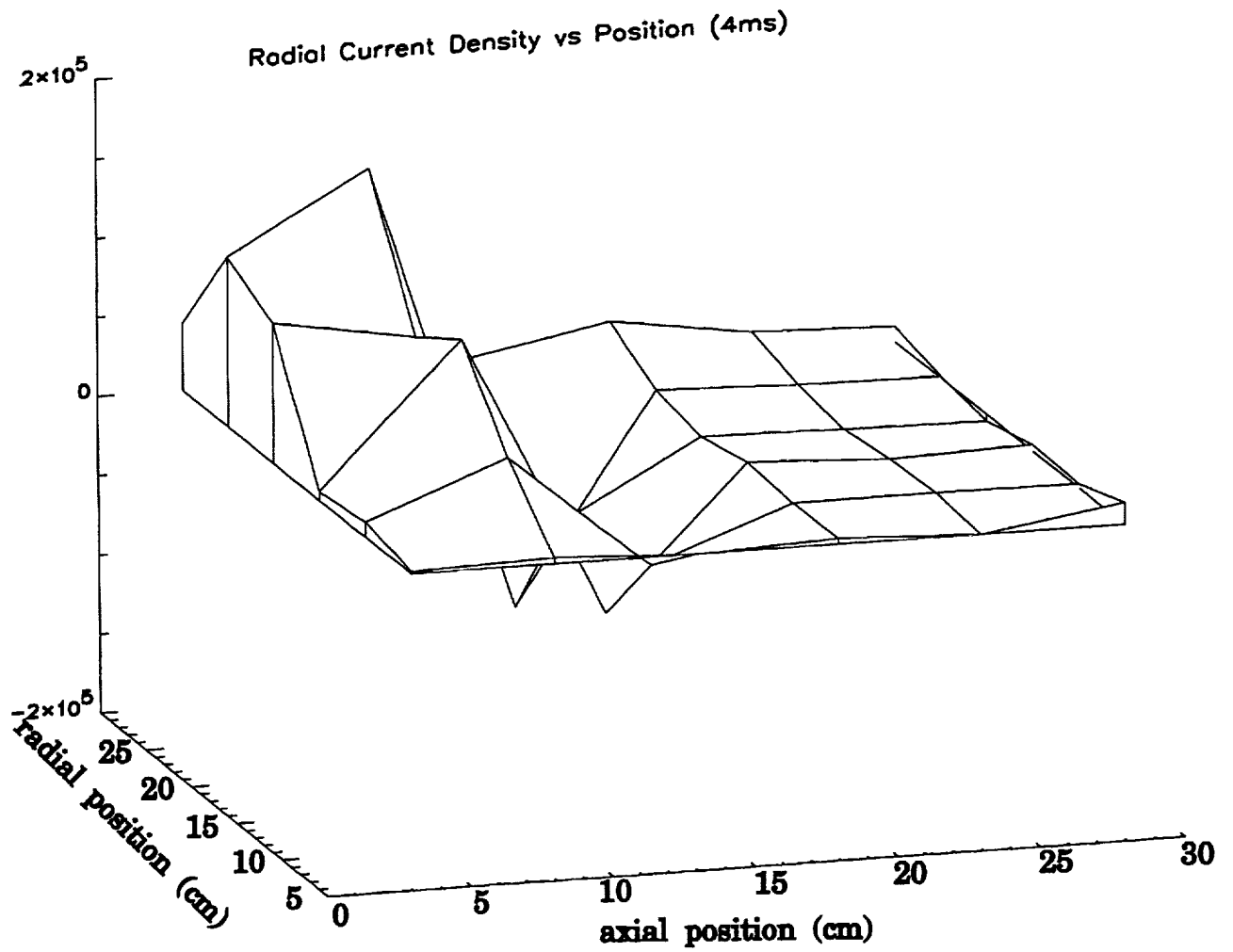
Figure 14 (b). Radial current density as a function of axial and radial position for a 6 MW discharge at t = 4 ms.
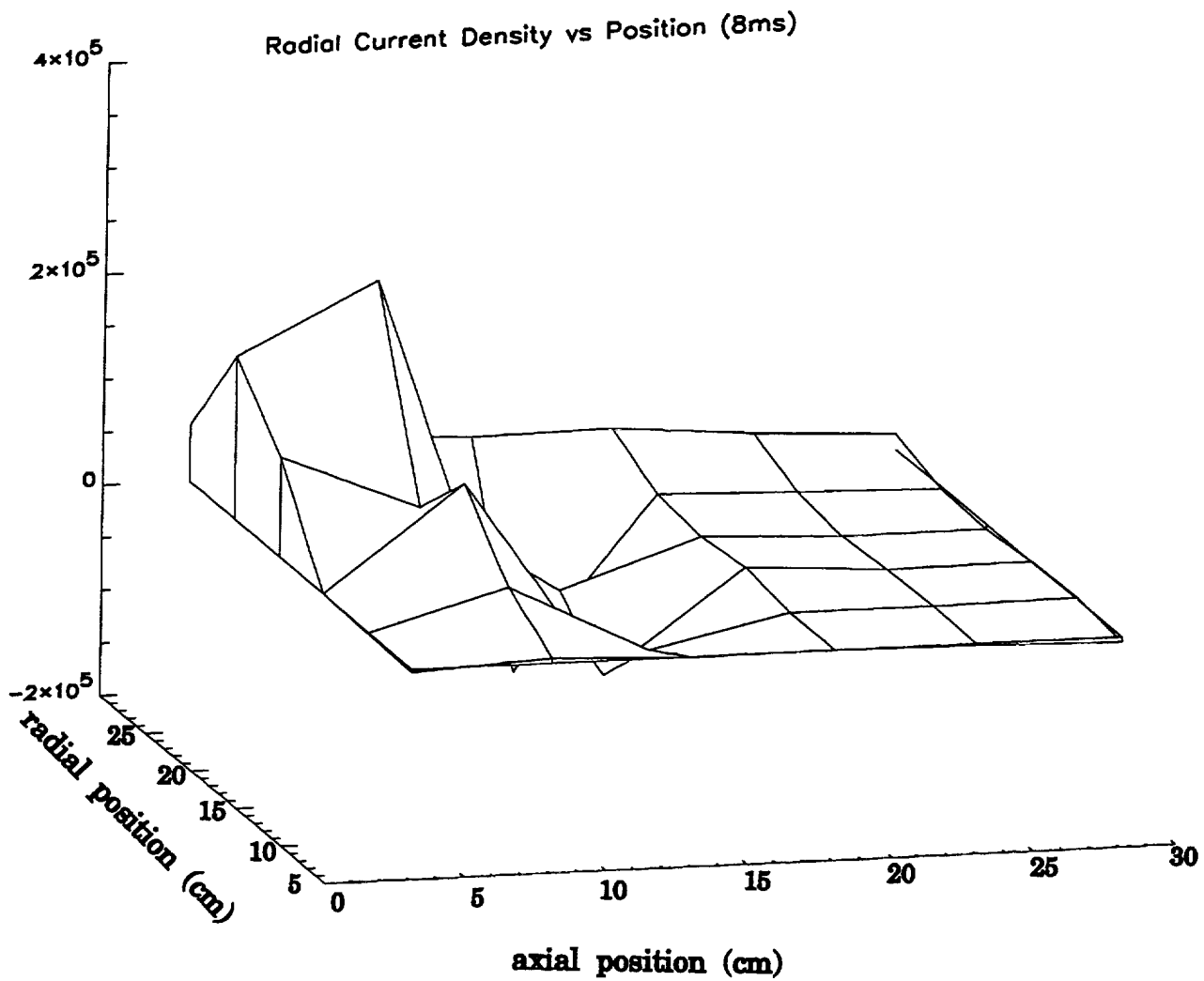
Figure 14 (c). Radial current density as a function of axial and radial position for a 6 MW helium discharge at t = 8 ms.
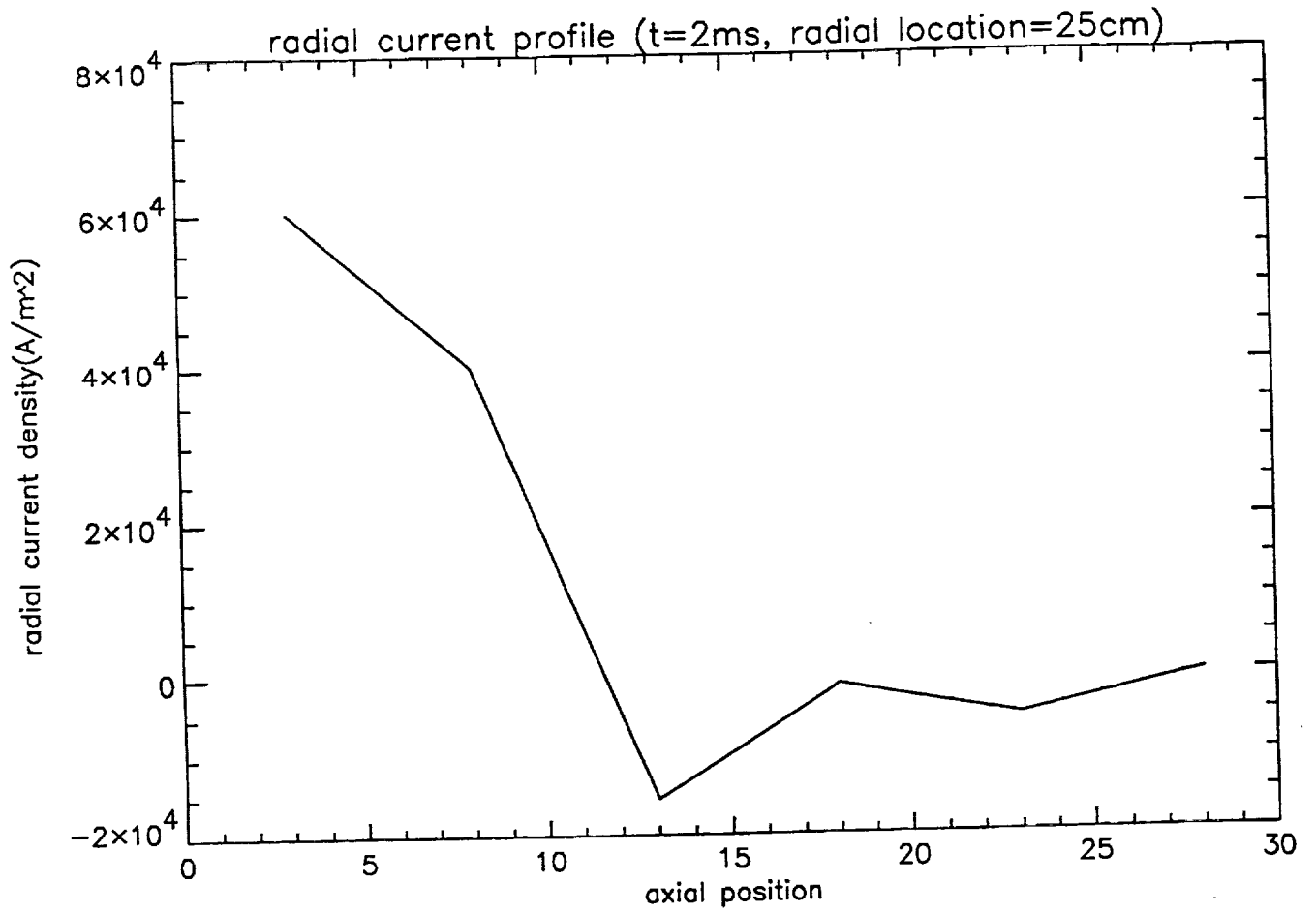
Figure 15 (a). Radial current density as a function of axial position at a radius of 25 cm for a 6 MW helium discharge at t = 2 ms.
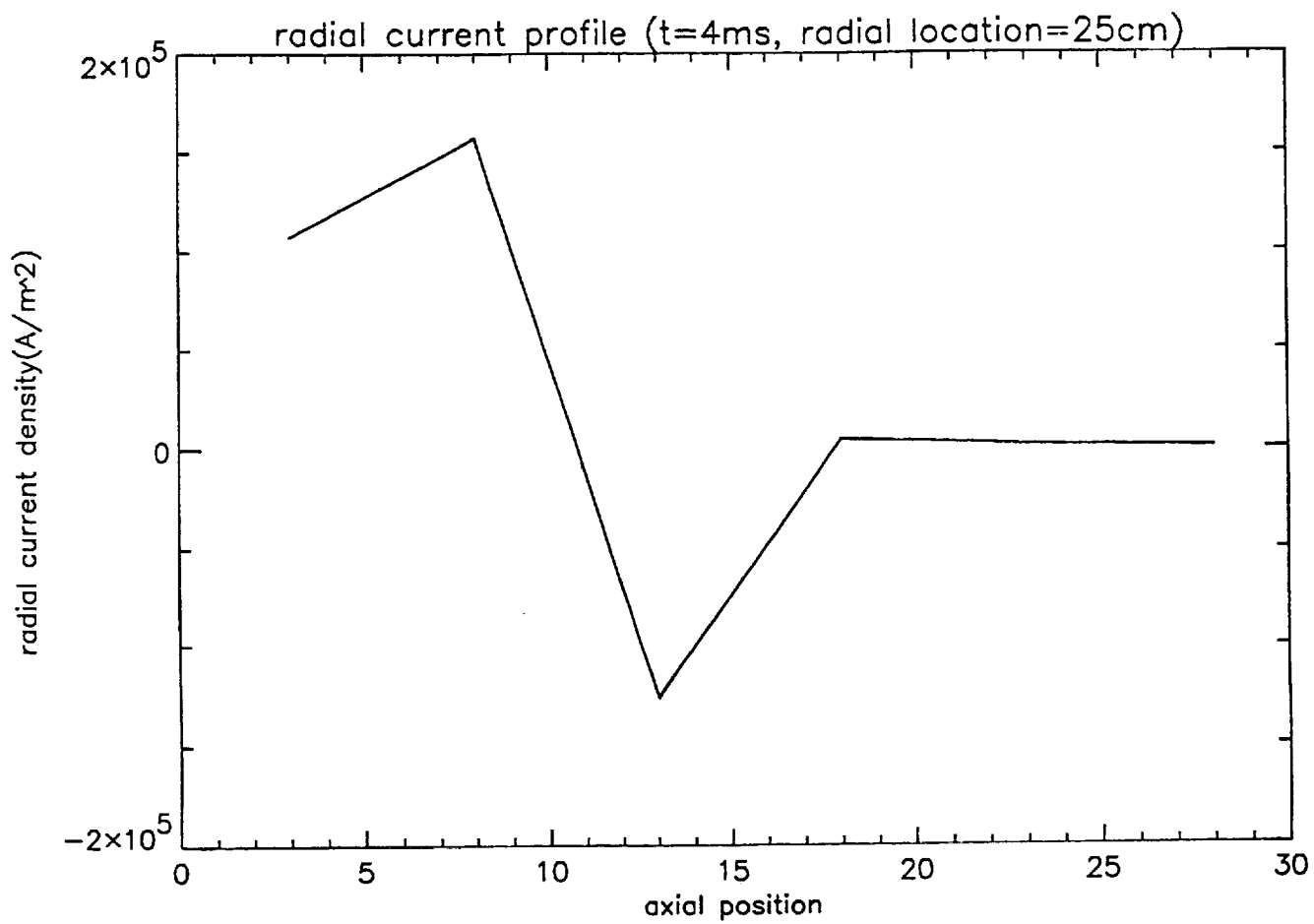
Figure 15 (b). Radial current density as a function of axial position at a radius of 25 cm for a 6 MW helium discharge at t = 4 ms.
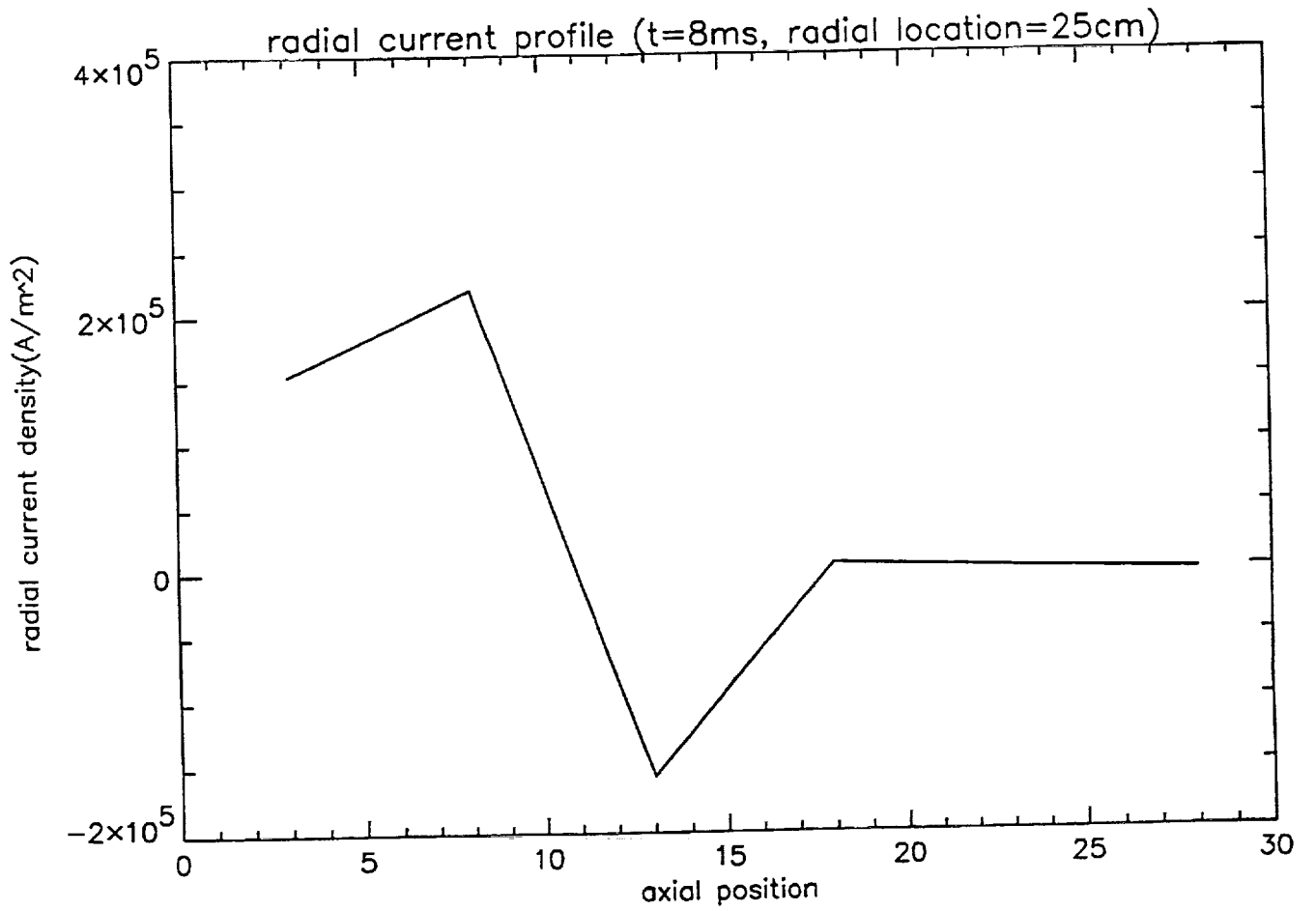
Figure 15 (c). Radial current density as a function of axial position at a radius of 25 cm for a 6 MW helium discharge at t = 8 ms.
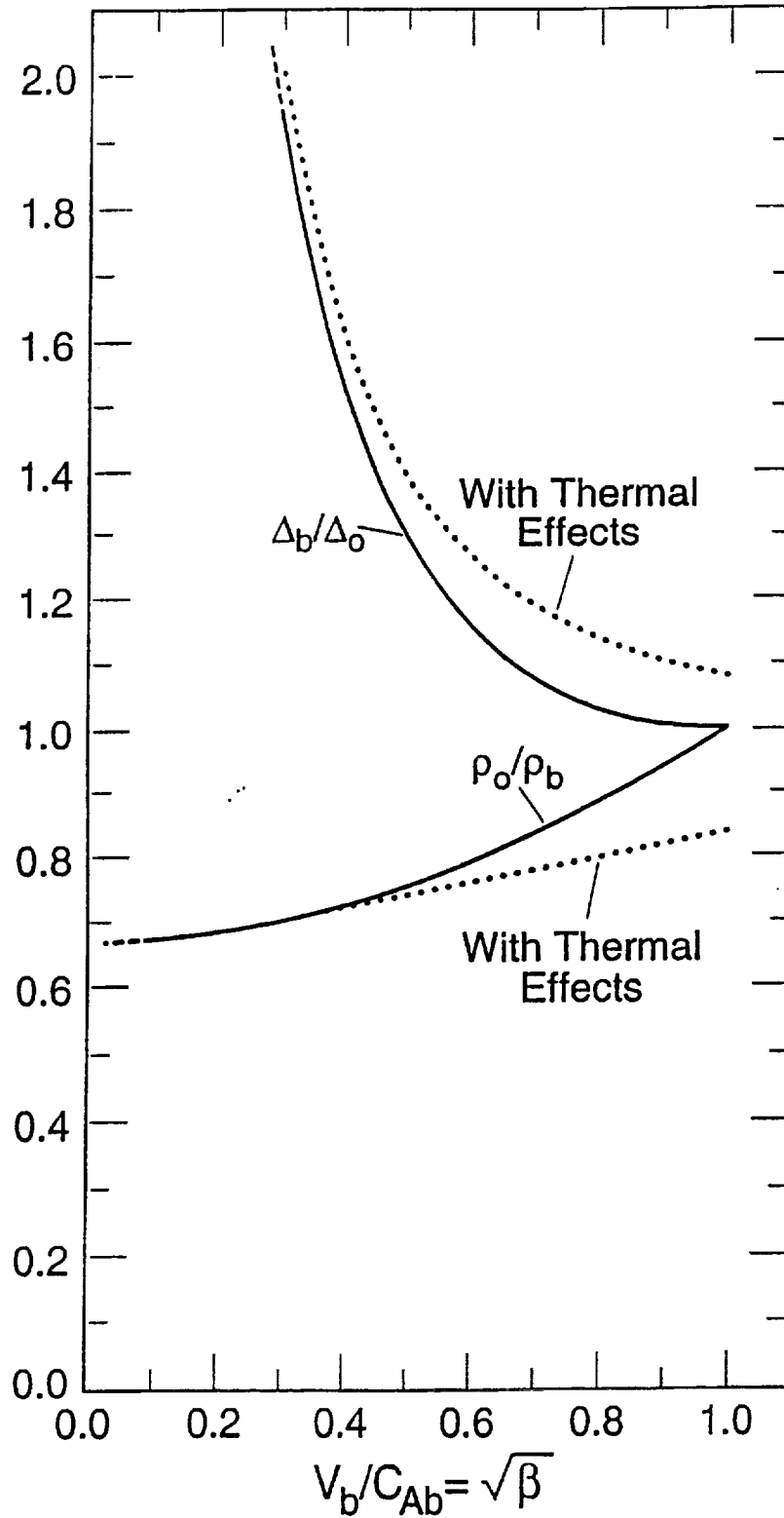
Figure 16. The nozzle contraction ratio (Δ_b/Δ_o) and the nozzle density ration (ρ_o/ρ_b) versus the upstream Alfvén-Mach number (V_b/C_{Ab}) in a self-field thruster, within ideal MHD.

REPORT DOCUMENTATION PAGE

1. AGENCY USE ONLY (Leave blank)	2. REPORT DATE April 1994	3. REPORT TYPE AND DATES COVERED Final Contractor Report

4. TITLE AND SUBTITLE

Performance of a Quasi-Steady, Multi Megawatt, Coaxial Plasma Thruster

5. FUNDING NUMBERS

WU–506–42–31
C–30065–A

6. AUTHOR(S)

Jay T. Scheuer, Kurt F. Schoenberg, Ivars Henins, Richard A. Gerwin, Ronald W. Moses, Jr., Jose A. Garcia, Robert F. Gribble, Robert P. Hoyt, Dorwin C. Black, and Robert M. Mayo

7. PERFORMING ORGANIZATION NAME(S) AND ADDRESS(ES)

Los Alamos National Laboratory
Los Alamos, New Mexico 87545

8. PERFORMING ORGANIZATION REPORT NUMBER

E–8723

9. SPONSORING/MONITORING AGENCY NAME(S) AND ADDRESS(ES)

National Aeronautics and Space Administration
Lewis Research Center
Cleveland, Ohio 44135–3191

10. SPONSORING/MONITORING AGENCY REPORT NUMBER

NASA CR–195311

12a. DISTRIBUTION/AVAILABILITY STATEMENT

Unclassified - Unlimited
Subject Categories 20 and 75

12b. DISTRIBUTION CODE

13. ABSTRACT (Maximum 200 words)

The Los Alamos National Laboratory Coaxial Thruster Experiment (CTX) has been upgraded to enable the quasi-steady operation of magnetoplasmadynamic (MPD) type thrusters at power levels from 2 to 40 MW for 10 ms. Diagnostics include an 8-position, 3-axis magnetic field probe to measure magnetic field fluctuations during the pulse, a triple Langmuir probe to measure ion density, electron temperature and plasma potential and a time-of-flight neutral particle spectrometer to measure specific impulse. Here we report on the experimental observations and associated analysis and interpretation of long-pulse, quasi-steady, coaxial thruster performance in the CTX device.

14. SUBJECT TERMS

Electric propulsion; MPD thrusters

15. NUMBER OF PAGES
84

16. PRICE CODE
A05

17. SECURITY CLASSIFICATION OF REPORT	18. SECURITY CLASSIFICATION OF THIS PAGE	19. SECURITY CLASSIFICATION OF ABSTRACT	20. LIMITATION OF ABSTRACT
Unclassified	Unclassified	Unclassified	